Cytoplasmic forces functionally reorganize nuclear condensates in oocytes

Adel Al Jord [1] ✉, Gaëlle Letort[1], Soline Chanet [1], Feng-Ching Tsai [2], Christophe Antoniewski[3], Adrien Eichmuller[1], Christelle Da Silva [1], Jean-René Huynh [1], Nir S. Gov [4], Raphaël Voituriez[5], Marie-Émilie Terret [1] & Marie-Hélène Verlhac [1]

Cells remodel their cytoplasm with force-generating cytoskeletal motors. Their activity generates random forces that stir the cytoplasm, agitating and displacing membrane-bound organelles like the nucleus in somatic and germ cells. These forces are transmitted inside the nucleus, yet their consequences on liquid-like biomolecular condensates residing in the nucleus remain unexplored. Here, we probe experimentally and computationally diverse nuclear condensates, that include nuclear speckles, Cajal bodies, and nucleoli, during cytoplasmic remodeling of female germ cells named oocytes. We discover that growing mammalian oocytes deploy cytoplasmic forces to timely impose multiscale reorganization of nuclear condensates for the success of meiotic divisions. These cytoplasmic forces accelerate nuclear condensate collision-coalescence and molecular kinetics within condensates. Disrupting the forces decelerates nuclear condensate reorganization on both scales, which correlates with compromised condensate-associated mRNA processing and hindered oocyte divisions that drive female fertility. We establish that cytoplasmic forces can reorganize nuclear condensates in an evolutionary conserved fashion in insects. Our work implies that cells evolved a mechanism, based on cytoplasmic force tuning, to functionally regulate a broad range of nuclear condensates across scales. This finding opens new perspectives when studying condensate-associated pathologies like cancer, neurodegeneration and viral infections.

Fertility depends on essential maternal transcripts and proteins accumulated during the growth of developing female germ cells known as oocytes[1]. In mammals, growing oocytes remodel their cytoplasm to position the nucleus at the cell center despite undergoing an asymmetric division in size, which relies on chromosome off-centering, soon after[2–4]. The central nucleus position predicts successful oocyte development in mice and humans[2,3], and thus, their embryogenic potential. However, the spatiotemporal evolution and the overall functional role of this cytoplasmic remodeling remain unclear.

Cytoplasmic remodeling is driven by cytoskeletal motor proteins[5]. Motor activity generates random fluctuating forces that stir the cytoplasm, enhancing nonspecific transport of organelles and their agitation in both somatic and germ cells[6–11]. In growing mouse oocytes, cytoplasmic random stirring is predominantly driven by F-actin and myosin-motor activity[9] with physical consequences observable on two spatiotemporal scales. On a large scale, prolonged cytoplasmic stirring displaces, nonspecifically, the 30-μm nucleus from the cell periphery to its center over a 25 μm distance[9,12]. On a smaller scale, cytoplasmic

stirring agitates the nucleus with stochastic kicks, resulting in nuclear membrane fluctuations and cytoplasmic force propagation inside the nucleus[10,11]. These forces enhance the mobility of the nucleolus[11], one of many nuclear liquid-like compartments of RNA processing known as biomolecular condensates[13–15]. We observed that, as growing mouse oocytes remodeled their cytoplasm, the number of nucleoli decreased in favor of a size increase (Fig. 1a–c), as noted long ago in human oocytes[16]. Moreover, fully grown oocytes mutant for the F-actin nucleator Formin2 and consequent capacity to stir their cytoplasm presented a peripheral nucleus enriched in multiple immobile nucleoli of smaller sizes (Fig. 1a–c, Supplementary Fig. 1a, and ref. 11). Since nucleoli as other liquid condensates can coalesce, this prompted us to investigate whether cytoplasmic forces during

oocyte growth orchestrated the reorganization of nuclear liquid-like condensates.

Here, we show that the cytoplasmic cytoskeleton in growing mouse oocytes can timely impose ordered scale-crossing changes in the internal organization of membrane-bound organelles like the nucleus. By stirring the cytoplasm and agitating the nucleus in oocytes, cytoplasmic forces remodel nuclear liquid-like condensates from the mesoscale down to the molecular scale. We demonstrate that force disruption decelerates the remodeling on both scales, whereas force-restoration reverses remodeling kinetics across scales. We then link the kinetics of condensate remodeling in the oocyte nucleus to altered molecular outputs during cell growth and an impact on subsequent meiotic cell division that drives fertility. Thus, oocytes deploy
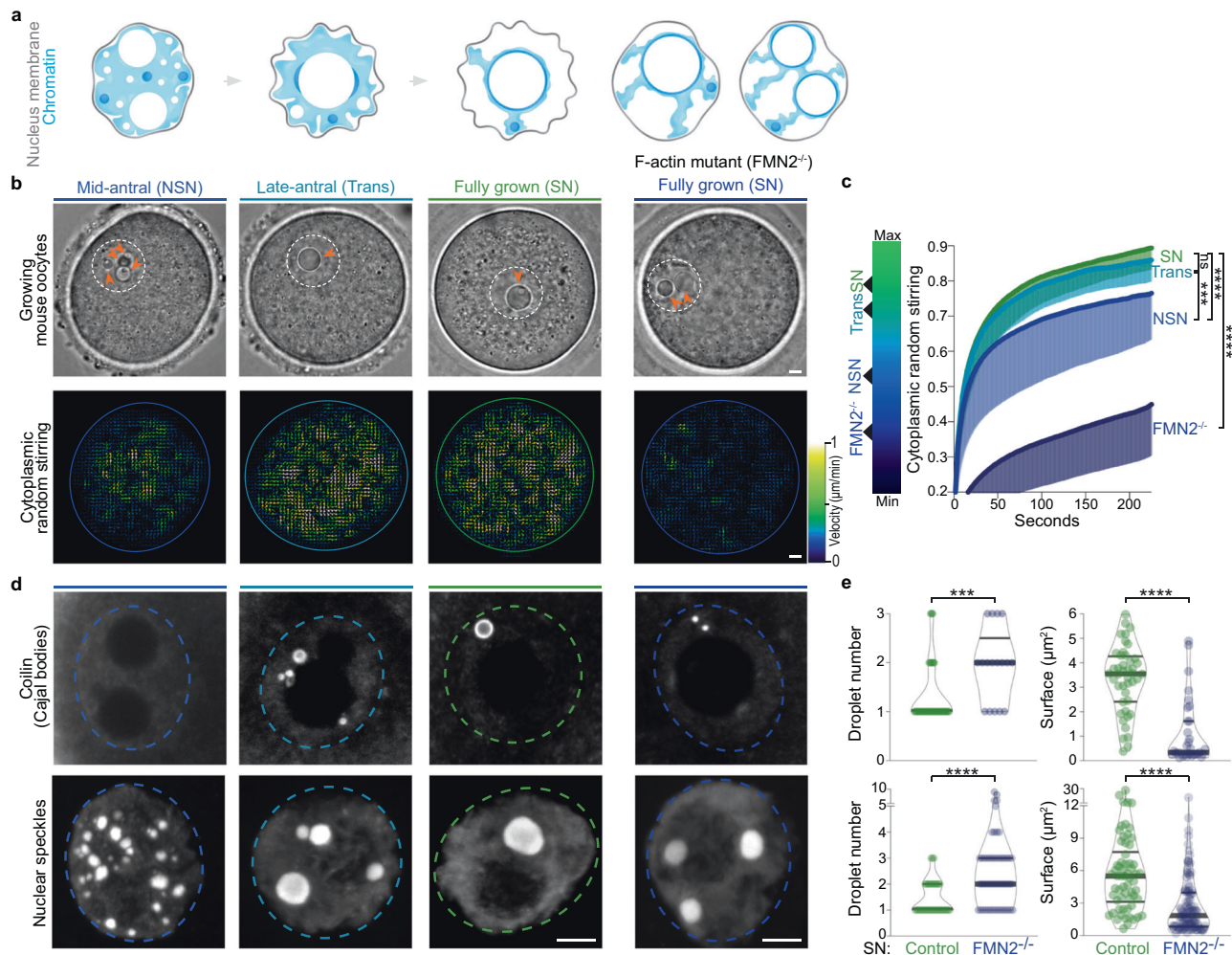

Fig. 1 | Nuclear biomolecular condensate patterns during mouse oocyte growth correlate with cytoplasmic remodeling. a Illustration of chromatin configuration evolution (non-surrounded nucleolus (NSN), transitioning (Trans), surrounded nucleolus (SN)) coinciding with oocyte growth subcategories (mid-antral follicle, late-antral follicle, and fully grown); (left) large spherical nucleoli decrease in number and increase in size as of the Trans-stage; (right) chromatin configuration scenarios in fully grown cytoplasmic F-actin mutants (FMN2^{−/−}) with one large or two smaller nucleoli. The nuclear membrane (gray) is depicted according to fluctuation intensity. **b** Top: Bright-field images of Control oocytes with growth progression and a fully grown mutant; the nucleus is in dashed white and orange arrowheads indicate multiple small nucleoli (NSN and FMN2^{−/−} SN) or a single large nucleolus (Trans and SN). Bottom: Growth-associated cytoplasmic stirring vector maps generated by STICS analyses of bright-field 240 s-stream videos; the oocyte cortex is outlined with colors reflecting the intensity of cytoplasmic stirring; maps are color-coded according to velocity magnitude (lowest in dark blue, strongest in

white). **c** Cytoplasmic random stirring intensity in time measured in Control NSN to SN and FMN2^{−/−} SN oocytes by image correlation analyses of cytoplasmic pixel evolution; color gradient (left) used in this study to represent cytoplasmic stirring intensity; cell number, Control NSN = 22, Trans = 19, SN = 28 cells, FMN2^{−/−} SN = 13; error bars represent mean-s.d. **d** Representative immunoreactivities of Coilin and nuclear speckles in growing Control oocytes and SN FMN2^{−/−} oocytes; Coilin images are 0.5 μm z-planes and nuclear speckle images are 20 μm z-projections; nucleus regions outlined with dashed circles. **e** Quantifications of Coilin (top) and nuclear speckle (bottom) droplet number and surface in nuclei of fully grown SN Control and mutant oocytes; Coilin, counted in 43 Control and 17 FMN2^{−/−} cells, measured 44 Control and 33 FMN2^{−/−} droplets; speckles, counted in 41 Control and 52 FMN2^{−/−} cells, measured 62 Control and 112 FMN2^{−/−} droplets; violin plots with median ± quartiles. P values derived from two-tailed Mann–Whitney U-tests, ns not significant, $P = 0.074$, ***$P < 0.0004$, ****$P < 0.0001$; color codes based on cytoplasmic stirring intensities; scale bars, 5 μm. Source data are provided as a Source Data file.

cytoplasmic forces to reorganize nuclear condensates across scales for developmental success. Furthermore, we reveal that actin-based or microtubule-based forces remodel nuclear condensates and that this condensate-remodeling capacity is evolutionary conserved. Our study highlights a functional mechanical link between active forces in the cytoplasm and biomolecular condensates in the nucleus, which, from a biophysical perspective, reflects the transduction of cytoskeleton-based active forces across different cellular domains and scales. We propose that this mechanism may be implicated in the progression of condensate-related diseases[17–22], several of which curiously associate with changes in cytoskeletal dynamics[6,23–26].

Results

Cytoplasmic forces intensify from the late-antral growth stage

To proceed, we first revised an oocyte late-growth classification method, solely based on progressive chromatin condensation[27], by linking it to a measure of cytoplasmic stirring and consequent nucleus position (Fig. 1a–c, Supplementary Fig. 1b–k, and Supplementary Movie 1). Growing oocytes extracted from antral follicles presented the three expected chromatin states in a nucleus of constant volume. Smaller mid-antral "NSN" oocytes (non-surrounded nucleolus) had relatively low cytoplasmic F-actin and stirred with an off-centered, poorly agitated nucleus, mirrored by moderate nucleus membrane fluctuations. Denser cytoplasmic F-actin and stronger cytoplasmic stirring were quantified in subsequent bigger late-antral "Trans" oocytes (Transitioning) that were in the process of nucleus centering. Comparably dense F-actin and equally intense stirring were measured in the cytoplasm of fully grown "SN" oocytes (Surrounded Nucleolus), with high cytoplasmic forces propagated onto a centrally positioned nucleus with a strongly fluctuating nuclear membrane. Thus, oocytes maximally intensify cytoplasmic stirring as of the Trans growth stage. This updated three-stage classification method, connecting known oocyte chromatin features with cytoplasmic stirring intensity, enabled us to inspect whether this cytoplasmic activity affects nuclear condensates in growing oocytes.

Force-increase correlates with nuclear condensate remodeling

To explore a global relation between cytoplasmic stirring and nuclear liquid condensates, we screened for diverse nuclear biomolecular condensates[14] in growing oocytes using known immunomarkers[28] of histone locus bodies, paraspeckles, gems, nucleoli, TDP-43 bodies, Cajal bodies, and nuclear speckles. Careful 3D examination of these condensates revealed their nuclear pattern evolution from the NSN to SN stages (Supplementary Fig. 2a, b). Further analyses demarcated condensates into two subpopulations with different properties. The first subpopulation of small shape-constrained condensates with stable chromatin association, insensitivity to the droplet dissolver 1–6-hexanediol[29], and incomplete fluorescence recovery after photobleaching (Supplementary Figs. 2c, d, 3a–h), collectively indicative of a non-liquid nature. The second subpopulation of large spherical and mobile droplet condensates that lacked apparent chromatin association dissolved in response to 1–6-hexanediol, fully recovered fluorescence post-bleaching, and rapidly coalesced (Supplementary Figs. 2c, d, 3a–i and Supplementary Movie 2–3), collectively indicative of liquid-like nature. We, therefore, focused on this second subpopulation of condensates to address our study's key question. We counted and measured various nuclear droplets in growing Control oocytes and in growing Formin2-mutant oocytes (FMN2⁻/⁻), that presents a significant drop in cytoplasmic stirring (Fig. 1d, e and Supplementary Fig. 4a–c). In Controls, Coilin (Cajal body), nuclear speckle, nucleolar, and TDP-43 droplets decreased in number and increased in size as growth ended. FMN2⁻/⁻ oocytes, however, had more numerous yet smaller Coilin, nuclear speckle, nucleolar, and TDP-43 droplets as they reached the fully-grown stage, despite Control-like total nuclear amounts of corresponding markers at tested growth stages (Supplementary Fig. 4d, e).

Other parameters known to modulate droplet sizes like cell and nucleus volume or neo-transcription were unaffected in mutants (Supplementary Fig. 4f–j). Thus, the intensification of cytoplasmic stirring in growing oocytes is linked to the spatiotemporal evolution of several nuclear liquid condensates, potentially through increased droplet coalescence dynamics.

Forces accelerate mesoscale remodeling of nuclear droplets

To confirm that cytoplasmic stirring enhanced nuclear droplet dynamics, we live-imaged at high temporal resolution growing oocytes microinjected with RNA encoding the nuclear speckle marker SRSF2-GFP. We chose speckles due to droplet abundance at all stages of growth and verified that SRSF2-GFP expression profiles were comparable to endogenous speckles. In all three stages of growth, we observed local droplet displacements and fusions instigated by the fluctuating nuclear membrane (Fig. 2a, Supplementary Fig. 5a, and Supplementary Movie 3), an immediate consequence of cytoplasmic stirring forces agitating the nucleus[11]. To estimate the magnitude of these local cytoplasmic forces agitating the nuclear membrane, we optically trapped cytoplasmic vesicles and pushed them against the membrane, artificially inducing comparable nuclear invaginations and droplet displacements with a force of the order of 10pN (Fig. 2b–d), in agreement with forces generated by multiple cytoskeletal motors in the oocyte cytoplasm[10]. Moreover, droplet diffusion was inversely proportional to its radius and correlated positively with the intensification of cytoplasmic forces during growth (Supplementary Fig. 5b, c). This was consistent with our hypothesis that cytoplasmic forces induce active diffusion of nuclear droplets (see Biophysical model in Methods). We, therefore, tuned the transmission of cytoplasmic forces to the nucleoplasm using established pharmacological and genetic tools[9,11], before monitoring droplet diffusion at distinct growth stages (Fig. 2e, f, Supplementary Fig. 5d, e, and Supplementary Movie 4). Amplifying nucleus agitation by disrupting force-dampening microtubules with Nocodazole[11] increased the effective diffusion of droplets at all stages when compared to Controls. Inversely, obstructing forces from the nucleus by Taxol-mediated stabilization of microtubules slowed down droplets. Greater deceleration occurred in cells with disrupted cytoplasmic actomyosin-based forces due to Cytochalasin-D incubation or FMN2 knockout. Depleting residual microtubule-based forces in FMN2⁻/⁻ oocytes with Nocodazole further diminished nuclear droplet diffusion. Droplet diffusion generally remained sub-diffusive (Supplementary Fig. 5f; $\alpha < 1$), consistent with chromatin-mediated constraints on droplet diffusion[30]. Thus, cytoplasmic forces, by agitating the nucleus, enhance the diffusive dynamics of nuclear droplets in constrained environments. Moreover, tuning nucleus agitation led to droplet size changes matching agitation intensity without affecting droplet shape or total SRSF2-GFP levels (Supplementary Fig. 5g–i). This suggested that cytoplasmic stirring, by enhancing droplet diffusivity, favored nuclear droplet encounters and coalescence.

To verify the cytoplasmic drive of nuclear droplet coalescence, we documented longer-term consequences of cytoplasmic stirring forces on nuclear droplet dynamics. 3D-tracking revealed stochastic displacements of droplets that bounced randomly around the nucleoplasm more vigorously as of the Trans-stage (Fig. 2g, h), concomitant with cytoplasmic stirring intensification. Droplets eventually encountered one another, collided and fused (Fig. 2i, Supplementary Fig. 6a, and Supplementary Movie 5). In FMN2-mutants, droplets bounced less frequently, and this decreased further when both F-actin and microtubules were disrupted (Fig. 2g–h and Supplementary Fig. 6b–d). We, therefore, modulated cytoplasmic forces and measured nuclear droplet coalescence kinetics in NSN oocytes that harbor significantly more droplets than SN counterparts (Fig. 2j, Supplementary Fig. 6e–g, and Supplementary Movie 6). Amplifying cytoplasm-based nucleus agitation accelerated droplet coalescence, manifested by a quicker decline in droplet number coupled with droplet size increase when compared to
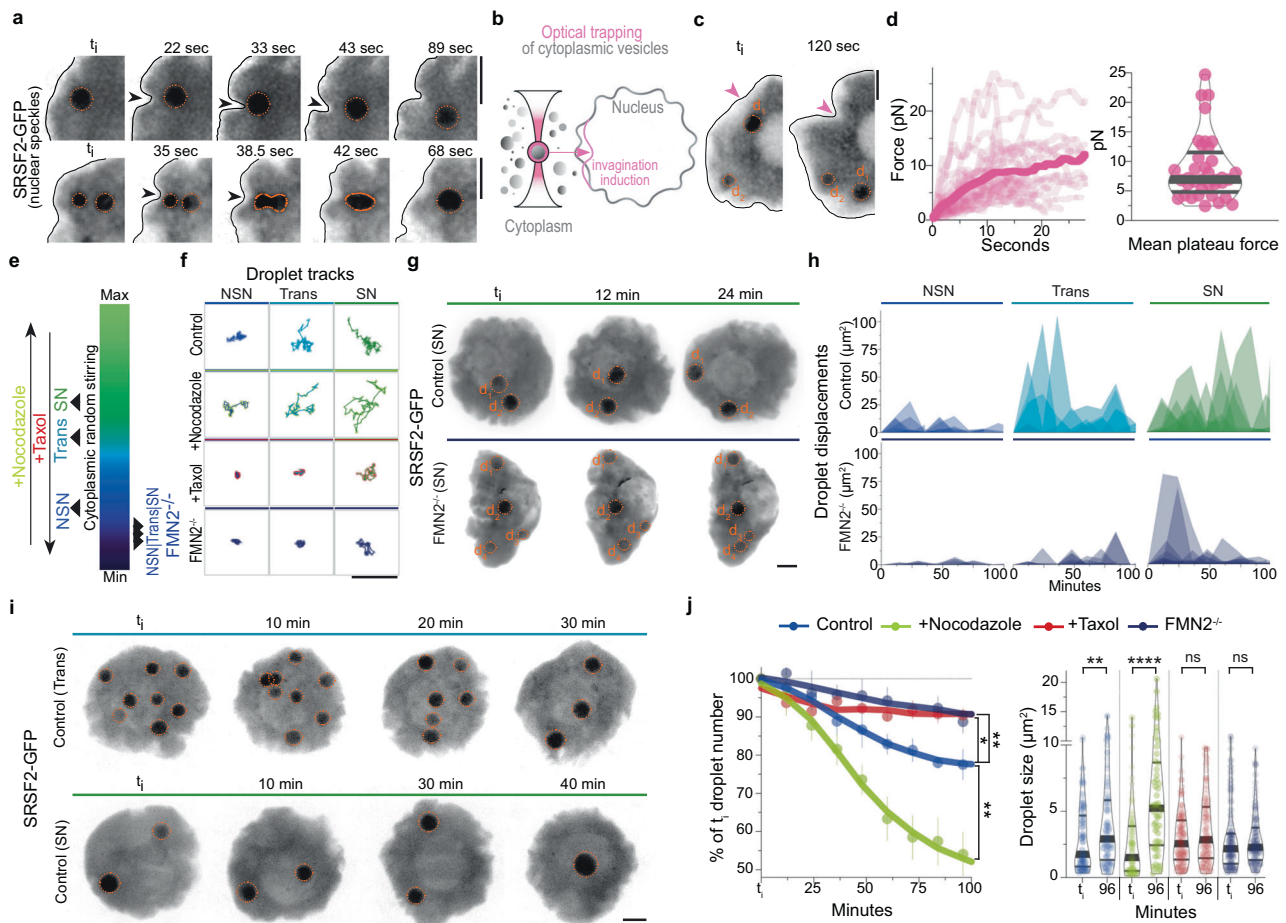
Fig. 2 | Cytoplasmic forces drive mesoscale condensate collision-coalescence in the nucleus. a Time-lapse images of nuclear membrane invaginations displacing nucleoplasmic SRSF2-GFP droplets in Trans (top) or NSN (bottom) cells; black arrowheads indicate nuclear membrane invaginations; membrane outlined in black. **b** Illustration of optical trapping experiment; cytoplasmic vesicles close to the nucleus were trapped and pushed against the nuclear membrane to exert forces and induce nuclear membrane invaginations. **c** Time-lapse showing a nuclear membrane invagination induced by the optical trapping approach, displacing a nucleoplasmic SRSF2-GFP droplet in a Trans cell; pink arrowhead indicates a point of contact between the trapped vesicle and nuclear membrane. **d** Individual force tracks in time (left) and mean plateau forces (right) obtained with optical trapping; 37 measurements from 20 oocytes. **e** Color gradient representing the intensity of cytoplasmic forces in growing Control and mutant oocytes or Controls treated with microtubule inhibitors. **f** Representative SRSF2-GFP droplet 2D-space exploration (50 s-tracks) at the three growth stages in Control oocytes, Controls incubated with Nocodazole or Taxol, and FMN2−/− oocytes. **g** Time-lapse 50 μm z-projections of SRSF2-GFP droplet displacements in the nucleoplasm of fully-grown SN Control

and FMN2−/− oocytes. **h** Fluctuating displacements of SRSF2-GFP droplets in Control and FMN2−/− oocytes at three stages of growth; droplet number in Control, NSN = 8, Trans = 5, SN = 6; in FMN2−/−, NSN = 12, Trans = 11, SN = 26. **i** Control SRSF2-GFP droplet dynamics (50 μm z-projections) in Trans and SN cells. **j** Nuclear SRSF2-GFP droplet collision-coalescence speed. (Left) nuclear SRSF2-GFP droplet number evolution (in % of initial droplet number) with Control, amplified (+Nocodazole), or disrupted cytoplasmic forces (+Taxol or FMN2−/−) in NSN oocytes; four oocytes per condition; error bars represent mean ± s.e.m.; P values derived from two-tailed Wilcoxon matched-pairs signed rank tests, *P = 0.0195, **P < 0.0078. (Right) nuclear droplet surface at the initial timepoint (t_i) and t = 96 min; droplet number, Control t_i = 113, t_{96} = 96, Nocodazole t_i = 93, t_{96} = 58, Taxol t_i = 114, t_{96} = 104, FMN2−/− t_i = 141, t_{96} = 124; violin plots with median±quartiles; P values derived from two-tailed Mann−Whitney U-tests, ns not significant, P > 0.177, **P = 0.0071, ****P < 0.0001. Droplets in **a**, **c**, **g**, and **i** are outlined in dashed orange; color codes based on cytoplasmic stirring intensities; scale bars, 5 μm. Source data are provided as a Source Data file.

Controls. Inversely, taming nucleus agitation decelerated droplet coalescence, revealed by weak droplet number decline and mean droplet size changes within the 100-min filming period. Chromatin remained in a decondensed state in analyzed cells (Supplementary Fig. 6h, i), hence eliminating the chromatin condensation bias potentially impacting droplet coalescence. Thus, cytoplasm-based agitation of the nucleus accelerates nuclear droplet collision-coalescence kinetics.

Forces are sufficient for nuclear droplet remodeling
To further dissect the cytoplasmic drive of nuclear droplet collision-coalescence, we built an agent-based model of SRSF2-like droplet diffusion in a nucleus-like spherical container agitated by cytoplasmic forces. Nuclear obstacles, based on experimental chromatin surface measurements, were added to mimic nuclear crowding by chromatin.

3D-numerical simulations were calibrated to recapitulate Control NSN nuclear droplet diffusive dynamics on the second's timescale (Fig. 3a). Unexpectedly, running these simulations on 100-min timescales reproduced experimental Control and modulated cytoplasmic drives of nuclear droplet coalescence in NSN oocytes (Fig. 3b, c). Thus, nuclear droplet diffusion and collision-coalescence propelled by cytoplasmic forces are sufficient to explain the observed droplet coarsening in the crowded nucleus.

Computational predictions of force-based droplet remodeling
To then estimate the minimal time necessary to reorganize nuclear compartments if cells were to transition from NSN to SN states of oocyte growth, a process occurring inside the follicle that cannot be followed in live, and to evaluate chromatin's interference with the
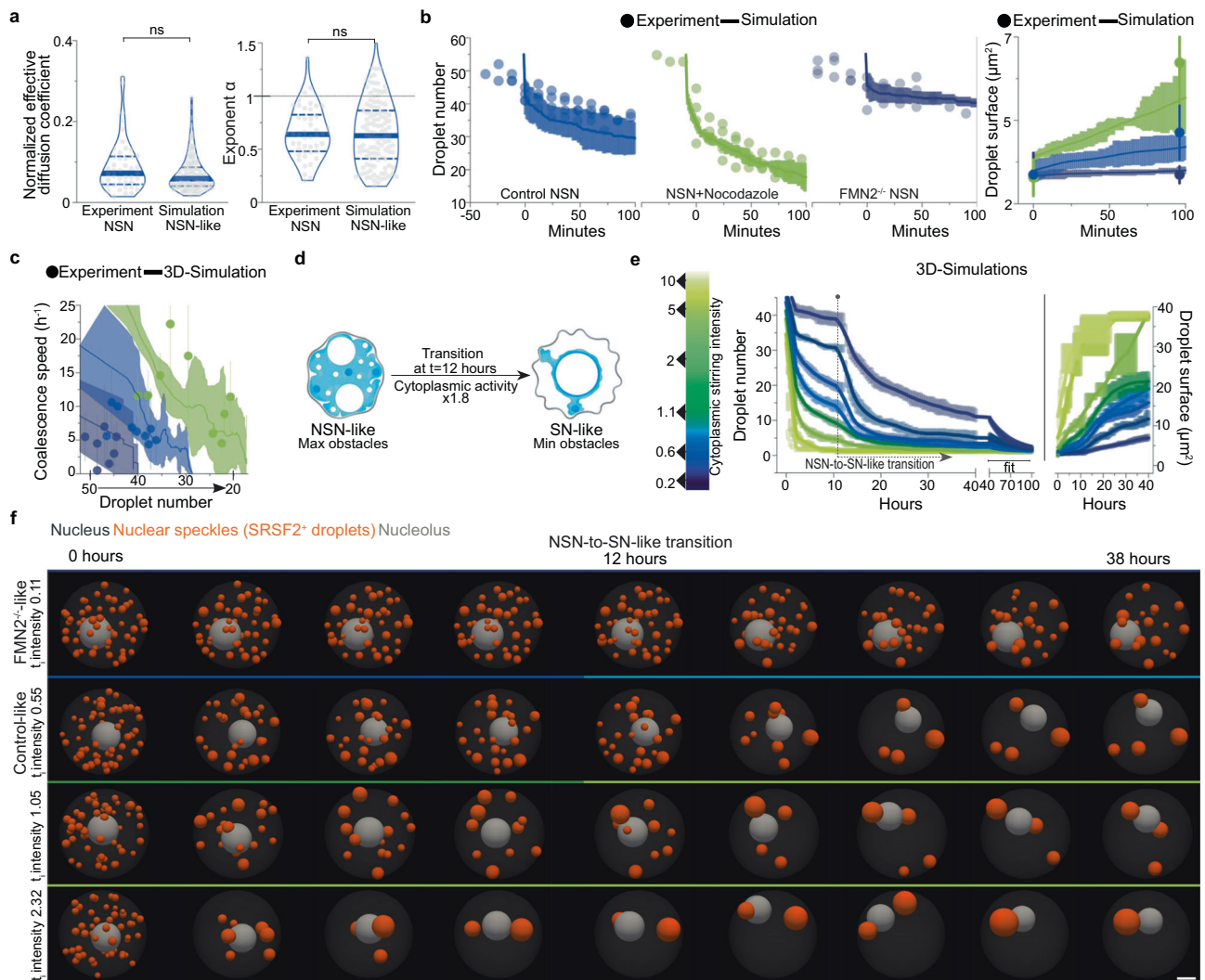
Fig. 3 | Computational models predict cytoplasmic forces to be predominant drivers of nuclear condensate remodeling. a Effective diffusion coefficients normalized by droplet size and droplet diffusive exponents α from SRSF2-GFP experiments (NSN oocytes) and simulations with NSN-like obstacles; droplet number, Experiment = 46; Simulation = 115; violin plots with median±quartiles; P values derived from two-tailed Mann–Whitney U-tests, ns not significant, $P = 0.1203$ and $P = 0.8741$. **b** Droplet number (left) and size (right) evolution in NSN-like simulations (lines) and in NSN-oocyte experiments (circles) for Control, Nocodazole, and FMN2$^{-/-}$ conditions; simulations and experiments were aligned on comparable time frames by defining 45 droplets as $t = 0$; simulations performed five times per condition and experimental data from four NSN oocytes per condition. **c** Nuclear droplet coalescence speed per hour relative to droplet number decrease in experimental NSN conditions (Control in blue, Nocodazole in green, and FMN2$^{-/-}$ in dark blue) and computational models with simulated NSN Control-like, Nocodazole-like, and FMN2$^{-/-}$-like cytoplasmic activity; error represents mean ± 95% confidence interval; the number of experimental measurements, Control NSN = 9, Nocodazole = 9, FMN2$^{-/-}$ = 7; 5 simulations per condition. **d** Schematic

representation of the NSN-to-SN-like simulation regime; first 12 h of simulations are performed with the same parameters as in NSN-like simulations; nuclear obstacle and cytoplasmic stirring activity switch occur at 12 h whereby 40% of chromatin-like obstacles surround the nucleolus and cytoplasmic activity is nearly doubled to mimic the transition into the SN-like condition, physiologically marked by chromatin condensation and cytoplasmic force intensification. **e** 3D-simulations ($n = 41$) showing nucleoplasmic SRSF2 droplet coalescence speed on an hour-to-day timescale relative to cytoplasmic forces (intensities colored according to the gradient on the left); simulations start from an NSN-like nucleus state with 45 SRSF2 droplets; chromatin condensation and cytoplasmic activity intensification, simulating the transition into late growth, occurs at 12 h. **f** Time frames of 3D-simulations in (**e**) with a gradient of starting point cytoplasmic intensities that include the FMN2$^{-/-}$-like and Control-like scenarios; nuclear speckles (SRSF2$^+$ droplets) are orange, and a gray nucleolus is depicted in a nucleus-like container. Color codes based on cytoplasmic stirring intensities; scale bar, 5 µm. Source data are provided as a Source Data file.

process, we ran our computational model on longer timescales (Fig. 3d–f, Supplementary Fig. 7a–c, and Supplementary Movie 7). To reproduce key physiological cytoplasmic and nucleoplasmic events that initiate at the end of oocyte growth, we incorporated into our simulations force intensification and chromatin condensation (Simulation series 2 with a transition at 12 h) that occurs after the NSN stage. To reach the endogenous compartmentalization state of 4 nuclear speckle droplets observed at the final growth stage (mean speckle droplet number in Trans cells with a central nucleus), Control oocytes would require 15 ± 8 h from the NSN|Trans transition. This prediction

is consistent with in vivo mid-to-end of antral oocyte growth, roughly estimated to occur within less than 2 days physiologically. The prediction is also consistent with prior experimental in vitro and computational studies since it falls within the time range of 5 to 17 h necessary for the cytoplasmic activity to displace the peripheral nucleus to the cell center[9,12]. By contrast, cells with diminished forces insufficient to transport the nucleus, such as FMN2$^{-/-}$ oocytes[9,12], would require at least 59 ± 8 h to reach a nuclear compartmentalization state comparable to Controls. These simulations also highlighted chromatin condensation-based acceleration of droplet fusion (compare before|

after $t = 12$ h in Fig. 3e), which would rationalize experimental observations of faster droplet diffusion in mutants that initiate chromatin condensation without intensifying cytoplasmic forces (Supplementary Fig. 5e). We, therefore, generated two supplementary models to weigh chromatin's interference with nuclear droplet kinetics (Series 1 and 3). We modeled an NSN nucleus state with decondensed chromatin and an SN nucleus state with condensed chromatin before launching simulations with force intensities maintained constant in time. Droplet collision-coalescence was faster in the condensed chromatin setup (Series 3), suggesting a kinetic barrier effect for chromatin coherent with its solid-like and diffusion-constraining properties[30,31]. Probing further, we found that with weak forces (FMN2^{-/-}-like scenario), chromatin significantly hindered droplet fusion, seen by the substantial drop in time required to coalesce all droplets post-chromatin condensation (Supplementary Fig. 7d; compare FMN2^{-/-} plain and dashed fits). In all Control-like scenarios, however, the forces reduced chromatin's hindrance to droplet fusion (Supplementary Fig. 7d; compare NSN, Trans, and SN plain and dashed fits). Thus, our simulations anticipate cytoplasmic force intensification to be a predominant driver of nuclear droplet coalescence in physiological contexts. Experiments and computations indicate that cytoplasmic forces in growing oocytes spatially reorganize nuclear liquid compartments by boosting large-scale droplet collision-coalescence.

Forces enhance sub-droplet and molecular scale kinetics

To determine local sub-droplet-scale consequences of cyto-to-nucleoplasmic force transfer, we first measured rapid surface fluctuations of large SRSF2-GFP droplets in Control and F-actin mutant SN oocytes±Nocodazole. Surface fluctuations of comparably-sized droplets declined when F-actin-based cytoplasmic forces were disrupted and decreased further after simultaneous disruption of both F-actin and microtubules (Fig. 4a and Supplementary Fig. 8a). The Control:mutant droplet fluctuation ratio ($\cong 2$) was smaller than the Control:mutant nuclear membrane fluctuation ratio ($\cong 6$ in ref. 11), in agreement with expected energy dissipation theorized by our biophysical model linking cytoplasmic stirring with the nucleoplasm (see Methods). This observable energy transfer of cytoplasmic forces onto nuclear droplets prompted us to evaluate the potential enhancement of droplets' internal molecular kinetics using FRAP (Fig. 4b, c and Supplementary Fig. 8b–e). Droplet molecules exchanged significantly slower in FMN2^{-/-} cells and cells treated with Cytochalasin-D than in Controls. Molecular dynamics in droplets were reversible after the restoration of cytoplasmic stirring by drug washout. To quantify the contribution of cytoplasmic active forces in driving nuclear dynamics across scales, we estimated a Péclet number P_n at the scale of droplet diffusion in the nucleoplasm down to molecular diffusion in the nucleoplasm and within droplets. This number can be defined here as the ratio of the expected diffusion coefficient resulting from active forces only, inferred from kinetic measurements of active fluctuations of the nuclear membrane and droplet surface to the observed diffusion coefficient that combines the response to both active stirring and thermal diffusion. Our calculations indicate that the active component is indeed potentially a significant contributor to driving the documented dynamics in the nucleus- from the diffusion of droplets in the nucleoplasm (P_n-5) down to that of molecules in the nucleoplasm (P_n-2.5) and within droplets (P_n-1.5) - as the energy of cytoplasmic active forces cascades across scales (see Biophysical model in Methods). Thus, cytoplasm-based agitation of the nucleus enhances nuclear sub-droplet-scale kinetics by amplifying droplet surface fluctuations and interior molecular mobility.

Molecular impact of scale-crossing droplet remodeling

Active fluctuations, such as the cytoplasmic ones transmitted onto nuclear droplets in oocytes, were recently proposed to enhance enzymatic catalysis[32]. Moreover, biomolecule mobility in condensates is expected to boost local biochemical reactions, which in nuclear speckles corresponds to, but is not limited to, mRNA processing by the spliceosome[33–35]. RNA-binding splicing regulators like the SR protein SRSF2 activate and alter splicing by binding specific regions of pre-mRNA known as exon splicing enhancers[36]. We, therefore, hypothesized that cytoplasmic active forces, by accelerating molecular dynamics in droplets, could enhance protein-RNA interaction kinetics that regulate splicing. To first test the splicing activation hypothesis, we immunostained growing oocytes using a specific phospho-marker pThr313-SF3b155 (pSF3b155), which was previously associated with catalytically active spliceosomes engaged in mRNA splicing[33,37]. Consistent with the general transcriptional decline during Control and mutant growth (Supplementary Fig. 4j), total nucleoplasmic levels of pSF3b155 decreased while total unphosphorylated SF3b155 remained comparable (Supplementary Fig. 8f–i). As opposed to the comparable transcriptional decline in both contexts, total nucleoplasmic pSF3b155 in mutants decreased more than in Controls as of the Trans-stage (Supplementary Fig. 8g). Since pSF3b155 was either droplet-associated or, when apparently nucleoplasmic, mainly chromatin-associated (Supplementary Fig. 8j), we compared droplet-associated to chromatin-associated signal ratios in Controls and mutants. Along with the transcriptional decline, pSF3b155 switched to mostly droplet-associated signal in both SN Controls and mutants (Supplementary Fig. 8k), while residual chromatin-associated pSF3b155 remained comparable (Supplementary Fig. 8l). This implied that the primary difference in pSF3b155 signal was found in nuclear droplets, prompting us to compare droplet-associated pSF3b155 in growing Control and mutant oocytes. The intensity of pSF3b155 remained unexpectedly constant in Control droplets while it dropped in droplets of mutants as of the Trans-stage (Fig. 4d, e). Since cytoplasmic stirring in Controls intensifies as of the Trans-stage, this suggested that cytoplasmic force-intensification sustains the pSF3b155 signal, specifically in nuclear droplets.

To next test the alternative splicing hypothesis, we performed splicing-centered bioinformatic analyses of mRNA-sequencing data comparing Control with mutant SN oocytes[11], the stage during which the observed pSF3b155 decline was maximal. We detected thousands of exon usage differences in mutant oocytes with 1785 overrepresented and 948 underrepresented exons (Fig. 4f and Supplementary Data 1), suggesting alternative splicing with enrichment of exon inclusion that is compatible with the idea of disrupted SR protein-RNA binding[38]. To probe the mRNA-processing imbalance further, we scrutinized differential transcript isoform usage, a direct consequence of alternative splicing, and uncovered hundreds of isoform switches in mutant oocytes (Fig. 4g and Supplementary Data 2). Multiple differential splicing events per transcript were identified for a sum of 3565 alternative splicing patterns of different subtypes in 1259 transcripts, with 2178 predicted consequences on transcript length or stability (Fig. 4h, i and Supplementary Fig. 9a). We confirmed some splicing pattern changes with RT-qPCR (Supplementary Fig. 9b–d). Supplementary enrichment and spatial correlation tests revealed that: altered exons and transcripts were significantly enriched in SRSF1 and SRSF2 binding sites; and altered splicing sites significantly overlapped with SRSF1 and SRSF2 sites up to 35 times more than other RNA-binding proteins, including the muscle-specific splicing factor MBNL3[39] or the RNA-binding transcription factor YY1[40] (Fig. 4j and Supplementary Data 3). Consistent with our hypothesis, these data suggest that cytoplasmic forces enhance SR protein-RNA binding kinetics in nuclear droplets and perhaps the binding kinetics of other splicing regulators nearby.

To finally confirm the mechanistic link between cytoplasmic forces and splicing, we expressed FMN2 in FMN2^{-/-} SN oocytes to restore cytoplasmic stirring. In these oocytes with rescued forces, multiscale kinetics of nuclear droplets were restored as well as their number and size within 5 h (Fig. 4b, c and Supplementary Fig. 9e–k). The intensity
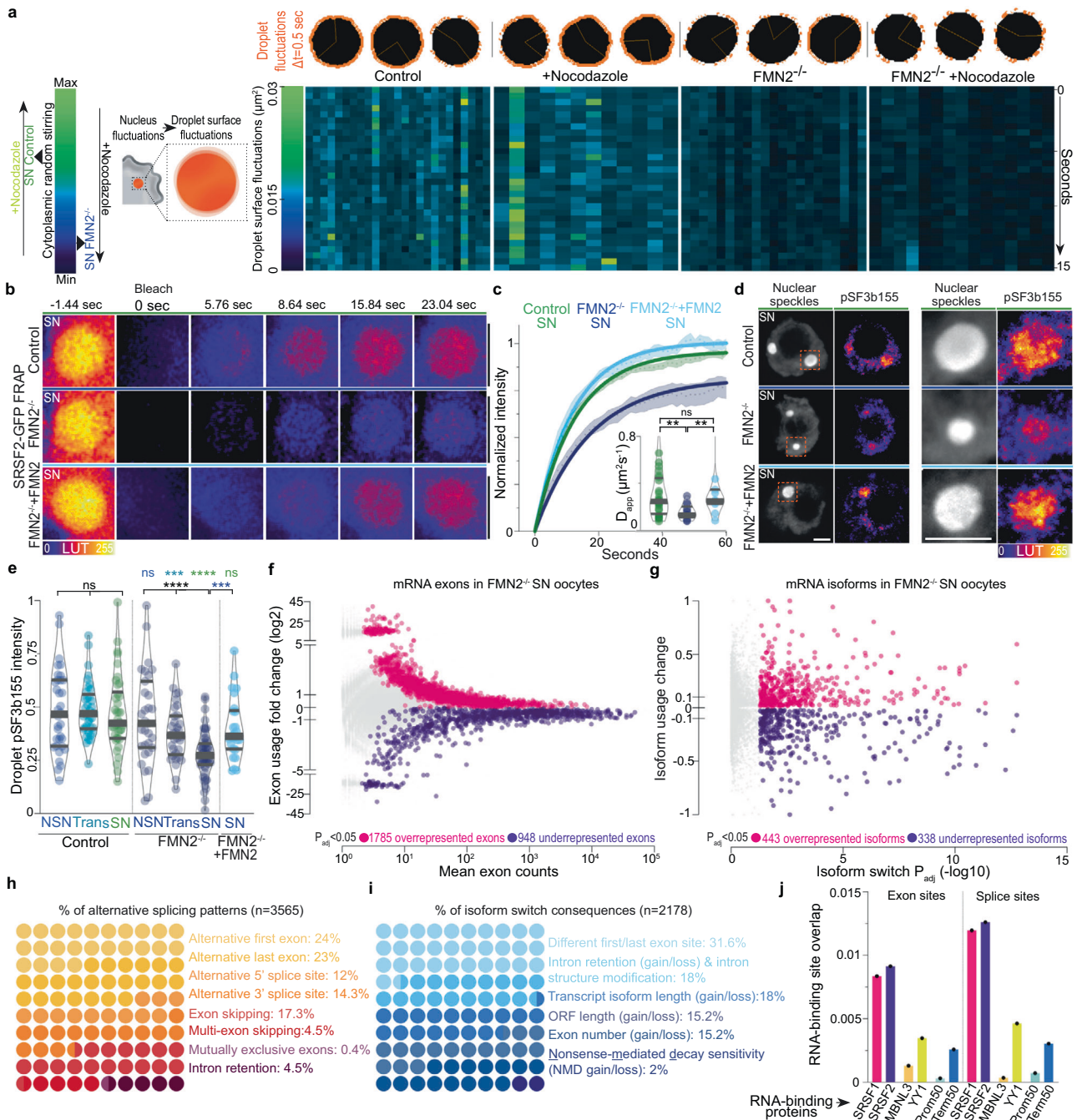
Fig. 4 | Cytoplasmic forces accelerate molecular-scale kinetics in nuclear condensates and regulate mRNA processing. a Scheme of droplet surface fluctuations as a function of cytoplasmic stirring (left); representative nuclear SRSF2-GFP droplet surface fluctuations in orange (above) and surface fluctuation intensity heatmaps of comparably-sized droplets (below) in SN oocytes with Control, amplified, or disrupted cytoplasmic forces; droplet radii, 2 to 2.7 μm; droplet number, Control = 25; Nocodazole = 12; FMN2$^{-/-}$ = 21; FMN2$^{-/-}$ + Nocodazole = 15. **b** FRAP sequences of SRSF2-GFP droplets in Control, FMN2$^{-/-}$, and FMN2$^{-/-}$ + FMN2 SN oocytes. **c** Fluorescence recovery curves (mean ± s.e.m.) with simple exponential fits of SRSF2-GFP droplets in Control, FMN2$^{-/-}$, and FMN2$^{-/-}$ + FMN2 SN oocytes; insets, apparent diffusion coefficients (D$_{app}$); droplet number, Control = 28, FMN2$^{-/-}$ = 13, FMN2$^{-/-}$ + FMN2 = 11. **d** Representative co-immunostainings of nuclear speckles and phosphorylated SF3b155 (pT313) in SN Control, FMN2$^{-/-}$, and FMN2$^{-/-}$ + FMN2 oocytes with magnifications of single droplets. **e** Quantifications of droplet-specific pT313-SF3b155 intensities in growing Control and FMN2$^{-/-}$ oocytes, and in FMN2$^{-/-}$ + FMN2 SN oocytes; Droplet number, Control NSN = 34, Trans = 37, SN = 38, FMN2$^{-/-}$ NSN = 31, Trans = 33, SN = 56, FMN2$^{-/-}$ + FMN2 SN = 26. **f, g** Differential

mRNA exon usage versus mean abundance or differential mRNA isoform usage versus isoform switch P$_{adj}$ in SN FMN2$^{-/-}$ oocytes relative to Control SN FMN2$^{+/-}$ oocytes; Colored dots are over/underrepresented exons or isoforms in FMN2$^{-/-}$ oocytes with a BH-adjusted (exons) or FDR-adjusted (isoforms) P value P$_{adj}$ < 0.05. **h, i** About 10 × 10 dot plots showing percentages of mRNA alternative splicing patterns detected in FMN2$^{-/-}$ (n = 3565 patterns) and percentages of predicted consequences of mRNA isoform switches in FMN2$^{-/-}$ (n = 2178 consequences). **j** Jaccard measures of overlaps between sets of genomic sites, through computation of the ratio of their intersections to their union; differentially used exon sites and alternative splice sites of transcripts of FMN2$^{-/-}$ oocytes were tested bidirectionally for spatial correlation with SRSF1, SRSF2, MBNL3, YY1 RNA-binding sites, and against in silico controls corresponding to the 50 first (Prom50) or last (Term50) nucleotides of all RefSeqNCBI transcripts. Violin plots with median ± quartiles (**c, e**); P values derived from two-tailed Mann–Whitney U-tests (**c, e**) and Kruskal–Wallis tests (**e**); ns not significant, *P > 0.0678, **P < 0.0099, ***P < 0.0006, ****P < 0.0001; scale bars, 5 μm. Source data are provided as a Source Data file.
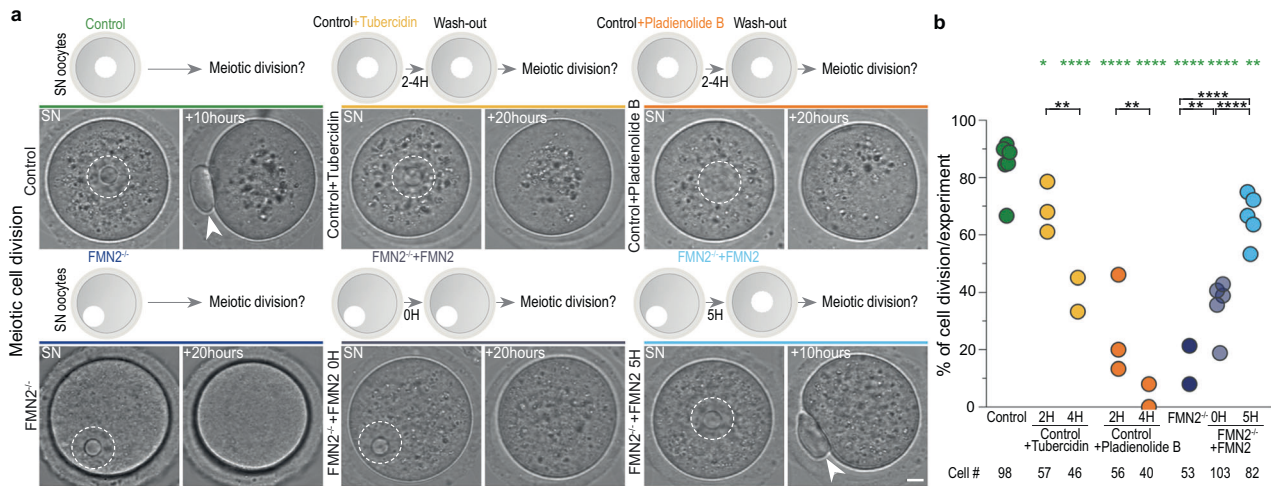
Fig. 5 | Cytoplasmic force-based regulation of mRNA processing drives meiotic cell division. a Assessment of the first meiotic division in Control, Control + Tubercidin, Control + Pladienolide B, FMN2$^{-/-}$, FMN2$^{-/-}$ + FMN2 0-h and 5-h rescue contexts; time-lapse images of Prophase SN stage oocytes 6 min prior to entry into division, measured by nuclear envelope breakdown, and 10 to 20 h after nuclear envelope breakdown with illustrations of each approach above; nuclei are outlined in dashed white; arrowheads indicate the extruded polar body, a readout of successful oocyte division. **b** Quantifications of successful oocyte division in Control, Control + Tubercidin, Control + Pladienolide B, FMN2$^{-/-}$, FMN2$^{-/-}$ + FMN2 0-h and 5-h rescue contexts shown in percentage of divided cells per experiment; cell number depicted below; P values derived from Fisher's exact test of proportions, *$P = 0.0245$, **$P < 0.0091$, ****$P < 0.0001$. Scale bar, 5 µm. Source data are provided as a Source Data file.

of pSF3b155 was also fully restored in droplets without affecting residual chromatin-associated pSF3b155 levels (Fig. 4d, e and Supplementary Fig. 9l), suggesting that cytoplasmic forces transmitted onto nuclear droplets enhance enzymatic catalysis in droplets. Splicing patterns were reversed to a certain extent with a mean rescue efficiency of ~60% (Supplementary Fig. 9b–d; compare rescue fold changes to mutant ones), which was expected due to the accumulation of mis-spliced transcripts prior to the rescue. Thus, cytoplasmic forces regulate mRNA processing, probably by enhancing splicing reactions in droplets of growing oocytes, with broad consequences on maternal reservoir transcripts.

Developmental impact of scale-crossing droplet remodeling

To evaluate the impact of splicing in fully grown oocytes on their development, we first treated Control SN oocytes with Tubercidin, an adenosine analog previously shown to disrupt nuclear speckles and alter splicing[41] (Fig. 5a, b and Supplementary Fig. 10a–j). This treatment gradually decreased droplet size, number, and associated pSF3b155 signal. Within 4 h, pSF3b155 in droplets decreased to FMN2-mutant levels and splicing was altered with comparable tendencies. We then washed-out Tubercidin and monitored the consequences on the meiotic division that directly ensues oocyte growth[1,4]. The treatments did not affect nuclear envelope breakdown but gradually hindered cell division. Cells that still divided did so with a significant delay, which is a poor prognostic of oocyte fitness. To confirm that this consequence on oocyte division was splicing-dependent, we treated Control SN oocytes with Pladienolide B, a potent spliceosome inhibitor specifically targeting the SF3b complex[42] (Fig. 5a, b and Supplementary Fig. 10a, b, h–j). Pladienolide B treatment altered splicing and, after washout, also caused cell division delay and failure. Since the large majority of splicing in SN oocytes is speckle-associated when assessed by pSF3b155, these data suggest that speckles and speckle-associated splicing can control the progression of oocyte division, which is consistent with studies linking speckles and speckle-associated splicing to the progression of somatic cell division[35,43–45]. These data also highlighted the importance of splicing in fully grown oocytes for the success of oocyte divisions, while indicating that cytoplasmic force-based regulation of splicing could potentially promote meiotic division.

To next seize the developmental impact of cytoplasmic force-based regulation of splicing, we first analyzed the functional enrichment of altered transcripts in FMN2-mutants. Genes concerned with mRNA-processing alterations were enriched for diverse cell division-related functions (Supplementary Data 4), in line with a role in oocyte divisions[1,4]. Moreover, the majority of these genes are translated during the first meiotic division[46] (Supplementary Data 5). We, therefore, probed whether compromised splicing in SN oocytes due to disrupted cytoplasmic forces affects the first meiotic division (Fig. 5a, b and Supplementary Fig. 10a, b). FMN2-mutant oocytes underwent nuclear envelope breakdown comparably to Controls yet predominantly failed to divide, confirming previous observations[47,48]. Mutant cells rescued with FMN2 yet with insufficient time to stir back their cytoplasm before entry into division also predominantly failed to divide. By contrast, restoring cytoplasmic stirring in mutant oocytes for a time sufficient to rescue nuclear droplets and splicing phenotypes led to successful divisions in a majority of cells. Thus, cytoplasmic forces in growing oocytes reorganize nuclear droplets across scales to drive subsequent meiotic success critical for fertility.

Cytoskeleton-based nuclear droplet remodeling is conserved

We finally assessed the evolutionary conservation of the cytoplasmic capacity to reorganize nuclear liquid compartments. We chose *Drosophila melanogaster* oocytes due to their well-described cytoplasmic stirring dynamics[49,50], yet whose consequences on the nucleus interior remain unexplored. We, therefore, immunostained nuclear speckles in mid-oogenesis *Drosophila* oocytes (stage 9) when the cytoplasm is randomly stirred by microtubules and buffered by an actin mesh[49,50], which is the exact opposite of mouse oocytes where microtubules buffer actin-based stirring of the cytoplasm[9,11]. Disrupting the buffering actin mesh precociously via genetic inhibition of two distinct F-actin nucleators Cappuccino or Spire (mouse FMN2 or SPIRE homologs), amplified microtubule-based stirring of the cytoplasm, and prematurely induced fast streaming (Fig. 6a, b), a known transporting mechanism that, in various animals, plants and fungi, is vital for reproduction or developmental growth and differentiation[49,51]. Premature fast streaming during growth consistently led to larger yet less numerous nuclear condensates by stage 9 when compared to Controls (Fig. 6c–e). Inversely, stabilizing the actin mesh by
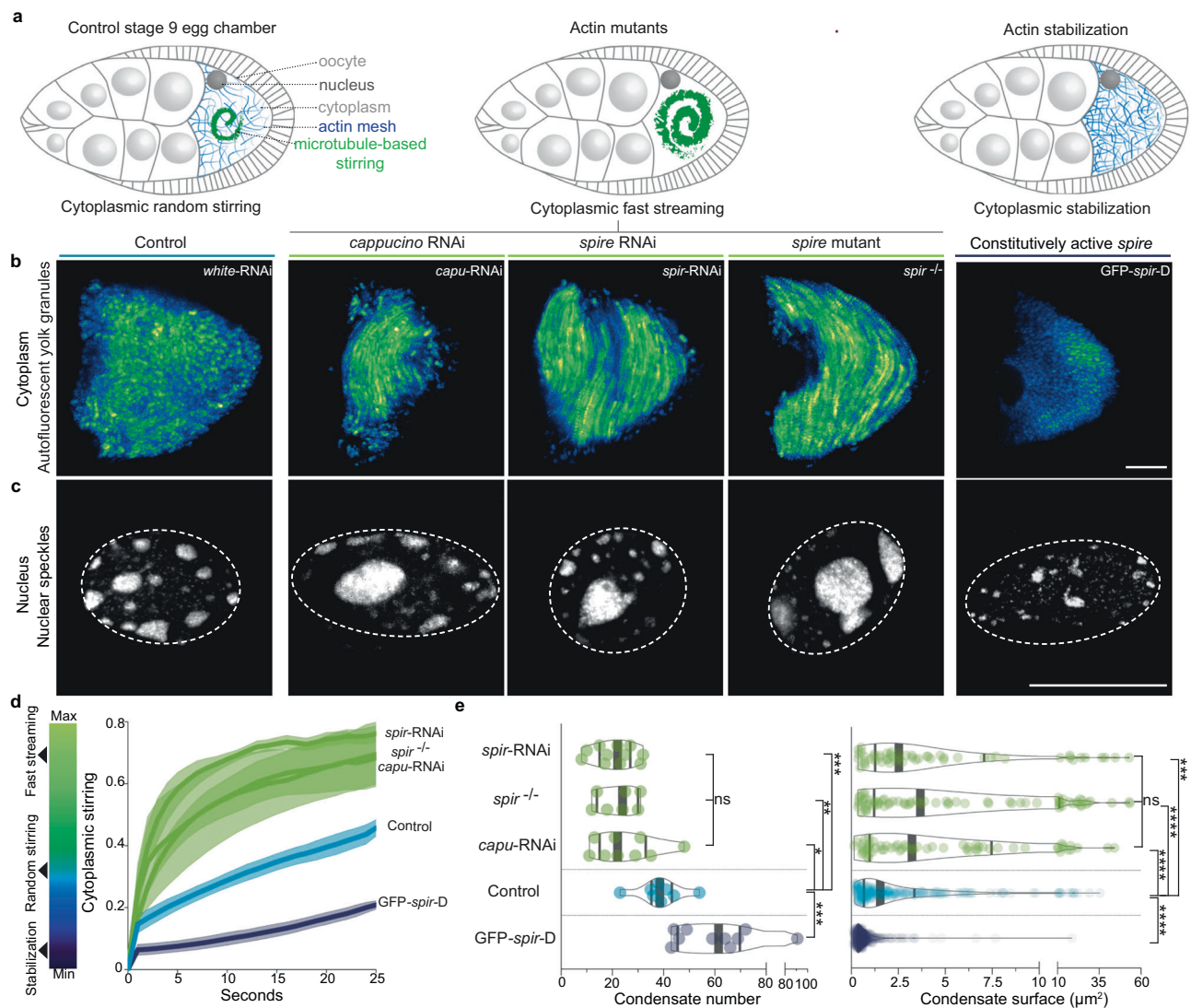
Fig. 6 | Cytoplasmic aptitude to reorganize nuclear condensates is evolutionarily conserved in insects. a Illustrations of *Drosophila melanogaster* stage 9 egg chambers composed of the oocyte surrounded by a nurse and follicular cells. At stage 9, cytoplasmic random stirring occurs in controls (left), premature microtubule-based fast streaming in actin mutants (center), and stabilization in mutants with constitutively active actin nucleators (right). **b** Time-projections of cytoplasmic stirring viewed with autofluorescent yolk granules in Control, *cappuccino*, and *spire* mutants, or constitutively active *spire* overexpression mutants (GFP-*spir*-D); single z-slice time-projections of 25 s shown with "GFB" LUTs. **c** Immunoreactivity of speckles in nuclei of oocytes with Control cytoplasmic random stirring, amplified fast streaming, or stabilization; 2 μm z-projections with nucleus regions outlined in dashed white. **d** Cytoplasmic stirring intensity measured in Control and mutant oocytes by image correlation analyses of cytoplasmic pixel evolution; cell number, Control = 4, *cappucino* RNAi = 3, *spire* RNAi = 5, *spire*^{-/-} = 3, GFP-*spir*-D = 2; error bars represent mean ± s.e.m. **e** Quantifications of nuclear speckle number and surface in control and mutant oocytes; cell number, Control = 8, *cappuccino* RNAi = 9, *spire* RNAi = 11, *spire*^{-/-} = 7, GFP-*spir*-D = 10; Condensate number, Control = 236, *cappuccino* RNAi = 62, *spire* RNAi = 55, *spire*^{-/-} = 74, GFP-*spir*-D = 437; violin plots with median ± quartiles; *P* values derived from two-tailed Mann–Whitney *U*-tests or Kruskal–Wallis tests, ns not significant, *P* > 0.576, *P* = 0.0121, **P* = 0.0037, ***P* < 0.001, ****P* < 0.0001. Scale bars, 20 μm. Source data are provided as a Source Data file.

overexpressing a constitutively active Spire blocked cytoplasmic stirring in growing oocytes[49] that, by stage 9, coherently lacked large nuclear condensates and showed enrichment of smaller condensates (Fig. 6a–e). Thus, cytoplasmic actin-based random forces, as in mouse oocytes, or microtubule-based random or streaming forces, as in fly oocytes, can boost nuclear condensate fusion. Moreover, the cytoplasmic capacity to refashion nuclear liquid compartments is evolutionary conserved and could potentially be deployed by other distant species for similar purposes.

Discussion

This multidisciplinary study uncovers that growing mouse oocytes remodel their cytoplasm to enhance nuclear condensate kinetics concurrently across scales for developmental success (Supplementary Fig. 10k). Cytoplasmic stirring forces function simultaneously as nuclear condensate colliders, boosting mesoscale reorganization in the nucleus, and as condensate core particle accelerators, enhancing molecular-scale dynamics within condensates. This scale-crossing reorganization of the nucleus ensures the success of the ensuing meiotic division, thus conditioning optimal oocyte development for fertilization[1]. This kinetic link between cytoplasmic remodeling and functional nuclear condensate reorganization rationalizes why cytoplasmic remodeling and its consequent nucleus positioning in mammalian oocytes is such a consistent predictor of their embryogenic potential[2,3]. We, therefore, expect this finding to guide future frameworks of reproductive efforts that include human in vitro fertilization and oocyte somatic cell nucleus transfer[52] for agricultural reproductive cloning or endangered species conservation.

Cells can thus physiologically deploy cytoplasmic active forces to drive complex reorganization of nuclear condensates across scales, with potential consequences on condensate-associated biochemical activity tailored to cell fate. This coordinating mechanism couples spatial reorganization of condensates at the mesoscale with molecular-scale changes within the same condensates, hence providing a concrete mechanistic example to recent speculations linking different condensate-associated length scales[15]. Active force fluctuations, such as the ones generated by the cytoplasmic cytoskeleton, were proposed to enhance biochemical reactions[32]. The transmission of active fluctuations onto liquid-like nuclear speckles and increase in speckle-associated pSF3b155 signal, a marker linked with catalytically active spliceosomes engaged in mRNA processing[33,37], suggest that cytoplasmic forces can timely optimize splicing reactions in nuclear speckles to drive subsequent cell division. Speckles, along with speckle-associated splicing, were previously linked to the progression of somatic cell division[35,43–45]. Thus, our findings further implicate nuclear speckles in cell division control while placing the cytoplasmic cytoskeleton as a potential upstream mechanokinetic coordinator of this cellular function.

Although we predominantly focus on how cytoplasmic forces regulate nuclear speckles in oocytes, our study implies the concomitant regulation of several other types of condensates as well as the evolutionary conservation of this mechanism. From an evolutionary advantage standpoint, deploying a single mechanism involving simple physical agitation of the nucleus indeed seems like an optimal solution to the complex problem of simultaneously regulating a variety of nuclear condensates along with their singular biochemical outputs. This physical mechanism is therefore likely to be relevant for other RNA-processing condensates in the nucleoplasm and other cell types in health or disease[13–15,17–22].

Methods

Animals and oocyte collection

Mice. All animal studies were performed in accordance with the guidelines of the European Community and were approved by the French Ministry of Agriculture (authorization N°75–1170) and by the Direction Générale de la Recherche et de l'Innovation (DGRI; GMO agreement number DUO-5291). Mice were housed in the animal facility on a 12-h light/dark cycle, with an ambient temperature of 22–24° Celsius and humidity of 40–50%. Mice used in this study include female OF1 (Oncins France 1; Charles River Laboratories; 8 to 12 weeks old), female C57BL/6 (Charles River Laboratories; 10 to 14 weeks old), and Formin2 (ref. 53) (FMN2$^{+/-}$ and FMN2$^{-/-}$; 8 to 16 weeks old). FMN2$^{-/-}$ males were crossed with FMN2$^{+/-}$ females to obtain both female Control FMN2$^{+/-}$ and Mutant FMN2$^{-/-}$ mice. At least two mice per experiment were used. Ovaries were extracted from mice as previously described[54] into pre-warmed (37 °C) M2 + Bovine Serum Albumin (BSA; A3311, Sigma) medium supplemented with 1 μM Milrinone[55], which maintains growing oocytes arrested in Prophase I. Ovarian follicles were punctured with surgical needles to release growing oocytes from antral follicles (end of oocyte growth[56,57]). Oocytes of different sizes were subsequently collected with a Stripper Micropipette (XLAB Solutions), washed, moved into dishes with fresh medium under mineral oil (M8410, Sigma), mechanically dissociated from follicular cells, and left to stabilize for an hour in the incubator at 37 °C before proceeding with experiments. Fully grown oocytes were washed 6 times with and transferred into fresh M2 + BSA medium without Milrinone to initiate oocyte in vitro maturation (IVM).

Drosophila melanogaster. The following stocks were used: v;; UASp−white-shRNA (BDSC #35573), v;; UASp−capu-shRNA (BDSC #32922), v; UASp−spir-shRNA (BDSC #43161), GFP-spirD (BDSC #24767), spir^{RP} cn^1 bw^1/CyO (BDSC #5113), b^1 pr^1 spir^{2F} cn^1/CyO (BDSC #8723). BDSC corresponds to Bloomington stock center. Flies were maintained on a standard medium in 25 °C incubators on a 12-h light/dark cycle. The white-shRNA was used as a control for knockdown experiments since white is not expressed during oogenesis. We used the nos-GAL4-VP16 driver (BDSC #64188) to perform knockdowns or overexpression in the germline. Knockdowns were performed at 29 °C to increase the efficiency of the GAL4 driver. 3-day-old females were collected and dissected in oil (10 S, Voltalef, VWR) for live imaging or in PBS1X for fixed experiments and stage 9 egg chambers were selected based on the morphology of the follicular epithelium.

Plasmids, in vitro transcription of complementary RNA (cRNA), and oocyte microinjection

Histone 2B-RFP (pRN3-H2B-RFP) was used to visualize chromatin (gift from C. Tsurumi[58]). SRSF2-GFP (a.k.a. SC35; NM_011358) was used to visualize nuclear speckles and was purchased from OriGene Technologies (MG202528). FMN2 (pCS2-FMN2-Myc[9]) was used to rescue cytoplasmic stirring in FMN2$^{-/-}$ oocytes. Plasmids were linearized with appropriate restriction enzymes. The T3 mMessage mMachine (AM1384, Thermo Fisher), SP6 mMessage mMachine (AM1360, Thermo Fisher), and T7 mMessage mMachine (AM13344, Thermo Fisher) transcription kits were used to synthetize capped cRNAs and purified with the RNAeasy kit (Qiagen) as previously described[59]. SRSF2-GFP and FMN2 RNA were polyadenylated using the Poly(A) Tailing kit (AM1350, Thermo Fisher). RNA concentrations were measured using a NanoDrop 2000 (Thermo Scientific). cRNAs were centrifuged at 4 °C for 60 min at 25,000×g before co-microinjection of 600 ng/μl SRSF2-GFP and 125 ng/μl H2B-RFP cRNA or 900 ng/μl FMN2 into Prophase I oocytes in 37 °C M2 + BSA + Milrinone medium using an Eppendorf Femtojet microinjector. Oocytes were then incubated for 2 h for SRSF2-GFP/H2B-RP cRNA translation or 0 to 5 h for SRSF2-GFP/FMN2 or FMN2 cRNA translation before proceeding with experiments. Exogenous SRSF2-GFP expression profiles were comparable to endogenous nuclear speckles. Note that FMN2 is degraded at meiosis resumption and resynthesized during the first meiotic division[48]. A potential difference of FMN2 amount at the end of meiosis I in the two rescue conditions (0 and 5 h) prior to meiosis resumption thus cannot explain the extent of each rescue in terms of successful cell divisions. This is rather due to the capacity of FMN2 to rescue cytoplasmic stirring and, consequently, cytoplasmic remodeling, nucleus position, nuclear speckle dynamics, and splicing activity before meiosis resumption.

Pharmacological inhibitors

The following inhibitors were used: 1,6-Hexanediol[29,60,61] (Hexanediol; 240117, Sigma-Aldrich) at 1 to 5%, Cytochalasin-D[62] (CCD; PHZ1063, Thermo Fisher) at 1 μM, Nocodazole (Noco; M1404, Sigma-Aldrich) at 1 μM, Paclitaxel[63] (Taxol; 580555, EMD Millipore) at 1 μM, Pladienolide B[42,64] at 10 μM (CAS 445493-23-2, SC-391691, Santa Cruz Biotechnology), and Tubercidin[41] at 10 μM (TO642, Sigma-Aldrich). Dimethyl sulfoxide (DMSO; D2650, Sigma) was used as a solvent for all inhibitors except Hexanediol before addition to M2 + BSA + Milrinone medium. Hexanediol crystals were directly dissolved in the medium at 37 °C before incubation with oocytes for 7 min (1% for Coilin and TDP-43) or 10 min (5% for nuclear speckles). Oocytes were washed three times in an inhibitor-supplemented medium and incubated for 60 min (CCD), 60 to 90 min (Noco, Taxol), or 120 to 240 min (Tubercidin, Pladienolide B) before proceeding. For droplet coalescence speed experiments, inhibitors were added 10 min before start of filming. For oocyte division experiments, oocytes were incubated in inhibitor-supplemented M2 + BSA + Milrinone medium for 2 or 4 h before washing out the inhibitors with M2 + BSA medium (without Milrinone) and proceeding with IVM in the incubator or the microscope chamber for up to 20 h.

Immunostainings

Mouse oocytes. Prophase I oocytes were incubated for 2 to 5 min with a 0.4% Pronase (P5147, Sigma) solution in M2 + BSA + Milrinone to dissociate the zona pellucida washed six times with fresh M2 + BSA + Milrinone medium, and maintained in it for 90 additional minutes. For detection of new transcripts, washed oocytes were incubated with 5-Ethynyl Uridine[65] (EU; 0.5 mM) from the Click-IT RNA Alexa Fluor-488 Imaging kit (C10329, Thermo Fisher) in M2 + BSA + Milrinone for 240 min. Before fixation, oocytes were washed three times in an M2 medium supplemented with PVP (P0930, Sigma) at 37 °C and placed on coverslips coated with gelatin and polylysine. Oocytes were then fixed without permeabilization in paraformaldehyde (PFA 4%; 18814, Polysciences or 15710, Electron Microscopy Sciences) at 30 °C for 30 min. After a PBS1X wash, oocytes were permeabilized and pre-blocked for 15 min with PBS1X with 0.5% Triton-X (93443, Sigma) and 3% BSA (A2153, Sigma) at room temperature before incubation with primary antibodies overnight at 4 °C followed by an hour incubation at room temperature with secondary antibodies. Primary and secondary antibodies were diluted in PBS1X with 0.2% Triton-X and 3% BSA. Cells were counterstained with DAPI (10 µg/ml; D9542, Sigma) for DNA observation and mounted in Prolong Gold antifade medium (P36941, Thermo Fisher) placed in 250 nm thick chambers (70366-12, Electron Microscopy Sciences) adhered to microscope slides (631–1554, VWR) to avoid oocyte squashing. EU revelation was performed before mounting according to the kit instructions. For F-actin visualization, oocytes were fixed as in (ref. 66) without Pronase treatment, labeled with Phalloidin conjugated with Alexa Fluor-488 (10 U/mL; A12379, Thermo Fisher), and mounted in Vectashield Antifade medium (H-1000, Vector Laboratories).

Drosophila melanogaster oocytes. Ovaries from 3-day-old females were dissected in PBS1X, fixed in PFA 4% for 20 min, permeabilized in PBT (0.2% Triton-X) for 30 min, left overnight with primary antibodies in PBT at 4 °C, washed three times 30 min in PBT, left with secondary antibody for 2 h at room temperature, washed three times 30 min in PBT and mounted in Citifluor medium (Electron Microscopy Sciences) for observation.

Antibodies. The following antibodies were used: rabbit anti-Coilin (1:2000; ab210785, Abcam), mouse IgG1 anti-Fibrillarin (1:60; ab4566, Abcam), mouse IgG1 anti-nuclear pore complex proteins MAb414 (1:1000; MMS-120P-100, Eurogentec), rabbit anti-NPAT (1:700; A302–772A, Bethyl Laboratories), mouse IgG1 anti-PSPC1(1:100; clone IL4, SAB4200503, Sigma-Aldrich), rabbit anti-pSF3b155 (phosphorylated at Thr313; 1:400; clone D8D8V, 25009, Cell Signaling), rabbit anti-SF3b155 (1:600; clone D7L5T, 14434, Cell Signaling), mouse IgG1 anti-SMN1 (1:100; Survival of Motor Neurons, clone 2B1, 05–1532, EMD Millipore), mouse IgG1 anti-SRSF2/SC35 (1:400; ab11826, Abcam), mouse IgG1 anti-TDP-43/TARDBP (1:1500; clone 3H8, MABN45, EMD Millipore), and species-specific Alexa Fluor secondary antibodies (1:400; Thermo Fisher). A recent study[45] proposed that the main target of the monoclonal SRSF2/SC35 antibodies is SRRM2 instead of SRSF2/SC35. However, SRRM2 is a spliceosome-associated protein that sharply localizes to nuclear speckles[45]. We also confirmed that the monoclonal ab11826 antibody we used recognized SRS2-GFP⁺ speckles in fixed oocytes expressing SRSF2-GFP. The conclusions of our study are thus unaffected by the proposed SRSF2/SC35 antibody discrepancy[45].

Microscopy

Mouse fixed and live imaging. Fixed and live mouse oocytes were examined with a Leica DMI6000B microscope equipped with a Plan-APO 40x/1.25 NA oil immersion objective, a motorized scanning deck and an incubation chamber (37 °C), a Retiga 3 CCD camera (QIimaging, Burnaby) coupled to a Sutter filter wheel (Roper Scientific), and a Yokogawa CSU-X1-M1 spinning-disk. Images were acquired using Metamorph (Universal Imaging, version 7.7.9.0) with 500 nm z-steps for a total of 40–50 µm in case of fixed cells and 1000 nm z-steps for a total of 35–60 µm in case of live cells. Oocytes were placed in a 35 mm tissue culture dish with cover glass bottom (FluoroDish FD35–100; World Precision Instruments) for video microscopy. Time-lapse 3D images were acquired at different time intervals (Δt = 5 to 12 min) with an exposition time of 500 ms for SRSF2-GFP and 300 ms for H2B-RFP. For high temporal resolution videos, Metamorph stream acquisition mode was used to capture cytoplasmic random stirring (in bright-field) and rapid diffusive dynamics of nuclear SRSF2-GFP droplets or their surface fluctuations (491 nm excitation wavelength) with a Δt of 0.5 s on a single z-plane focused on the nucleus or droplet center. For correlations between cytoplasmic stirring intensity and nuclear SRSF2-GFP droplet dynamics, oocytes were first filmed for 120 s in a bright-field and immediately followed by 120 s of filming with a 491 nm laser. For IVM experiments, oocytes were filmed in a bright-field with a Δt of 3 min on a single z-plane focused on the nucleus for up to 20 h. Supplementary Movies 2–4 and 6 were processed in FIJI (smooth and mean filter functions) for visual purposes only.

Optical tweezer setup. The custom-built optical tweezer system was generated by using a near-infrared fiber laser (1064 nm, 5 W, Ytterbium fiber laser, IPG Photonics, Oxford, Massachusetts) with a Nikon CFI Plan Apochromat Lambda, 100X, 1.45 NA, oil immersion objective (Tokyo, Japan) mounted on an inverted Nikon C1 Plus confocal microscope (Tokyo, Japan) as previously described in refs. 67,68. The setup is equipped with a temperature-controllable stage-top incubator (Tokai Hit STXG-WELSX, Gendoji-cho, Japan) that maintains cells at 37 °C in a humidified environment during experiments. Confocal images were acquired using a 488 nm solid-state excitation laser (Coherent, Santa Clara, California) with an ET525/50 bandpass filter (Chroma).

Positions of the trapped cytoplasmic vesicles were detected by recording the light pattern of the outgoing laser in the back focal plane of the condenser with a four-quadrant position-sensitive photodiode (QPD, Hamamatsu, Si PIN photodiode, Product No. S5981). The detected voltage values (V) were converted into displacements and forces by using the conversion value β (µm/V) and the trap stiffness κ (pN/µm)[69]. Ideally, one would determine the conversion value and the trap stiffness for every trapped vesicle. However, the complexity and heterogeneity of the cellular environment and the occurrence of multiple vesicles being trapped during experiments make it very challenging to do so. We thus determined the value of β by using a polystyrene bead with a diameter of 1 µm to represent the vesicles by following well-established methods[69]. Briefly, given that the optical trap was stationary, we moved a bead that was stuck to the glass bottom of the cell culture dish across the optical trap laterally by using a piezo stage (Nano-LP100, MadCityLabs, Madison, Wisconsin) while recording the output voltage signals by the QPD at 1000 Hz. Within a specific regime where the voltage output is linearly proportional to the stage displacement, we calculated the conversion value β = 1/0.192 µm/V. The trap stiffness was determined by the Boltzmann statistics method[69]. Briefly, we recorded the position distribution of a trapped vesicle by the QPD and then fitted a parabola to the logarithm of the distribution. We obtained trap stiffness κ = 12.8 pN/µm for both x and y directions assuming a symmetric trap. The advantage of the Boltzmann statistic method is that the drag coefficient of the trapped vesicle and the viscosity of the cytoplasm are not required.

To apply forces on the nuclear membranes, we used trapped cytoplasmic vesicles that were located close to the membranes. Given that the optical trap was stationary and the oocytes were immobile, settling on the bottom of the experiment dishes, we moved the piezo stage such that the membranes were moved towards the trapping center while the trapped vesicles were displaced away from the center.

Due to the trapping forces of the optical tweezers, the vesicles were then translocated towards the trapping center where membranes were localized, thus pushing against the membranes and consequently exerting forces on the membranes. To calculate the forces (F) exerted by the vesicles onto the membranes, we used the displacement of the vesicle according to Eq. (1):

$$F = \kappa \cdot (r - r_o) \qquad (1)$$

where r_o and r are the initial and final vesicle positions, respectively.

Fluorescence recovery after photobleaching (FRAP). For laser ablation experiments on SRSF2-GFP droplets, mouse oocytes were imaged at 37 °C with a Zeiss (Axio Observer.Z1/7) LSM 980 confocal microscope equipped with Airyscan 2, 2 PhotoMultiplier Tubes (PMT), a GaAsP spectral sensor, a Plan-APO 40x/1.3 oil immersion objective, a 488 nm 10 mW laser, and a motorized deck with a temperature-controlled chamber. Images were acquired using Zen 3.0 software. A total of 150 frames of 579 × 579 pixels (53 μm × 53 μm; 16-bit depth) were acquired on single z-planes with a bidirectional scan speed of 6 and 1.43 s intervals for a total of 214 s. Three frames preceded the bleaching (full 488 nm 10 mW laser power) of a fixed 8 μm × 2 μm region of SRSF2-GFP droplet-containing nucleoplasm. The bleached region size was fixed to be larger than the target droplet and thus included the neighboring dissolved SRSF2-GFP phase. Fluorescence recovery was imaged with 1.2% laser power.

***Drosophila melanogaster* fixed and live imaging.** Drosophila egg chambers were imaged with an inverted spinning-disk confocal microscope (Roper/Nikon) equipped with an sCMOS camera, with a 20X/0.75 objective for live egg chambers and a 60X/1.4 oil immersion objective for fixed egg chambers. Images were acquired with Metamorph with 1000 nm z-steps for a total of 30 μm in the case of fixed cells. To monitor cytoplasmic stirring, autofluorescent yolk granules in live oocytes were captured on single z-planes every 7 s using a 405 nm laser.

Quantifications and image analyses
Data were obtained from at least three independent experiments unless stated otherwise. All images were analyzed on Fiji (Version 2.0.0c-rc-69/1.52t). All graphs and statistical analyses were generated using MS Excel (Version 16.16.27) and GraphPad Prism 9.

Cytoplasmic stirring. The cytoplasmic stirring intensity in mouse and *Drosophila* oocytes was determined by image correlation analyses using a previously published software[9] and available on https://github.com/Carreau/OOCytes/tree/0.9. The software measures pixel changes between consecutive images. Raw time-lapse images (Δt = 0.5 s for mouse and Δt = 7 s for *Drosophila* oocytes) were first realigned using the Fiji StackReg plugin. In mouse oocytes, bright-field image correlations were calculated in 3 (NSN) or 4 (SN) cytoplasmic regions of 324 μm². In *Drosophila* oocytes, image correlations of autofluorescent yolk granules were calculated in 2 to 5 cytoplasmic regions of 441 μm². Correlation values from different regions within a cell were averaged. For visual clarity purposes, final correlation values were transformed by subtracting the value of each timepoint from 1 to obtain an inverted exponential-like curve.

Mouse oocyte cytoplasmic vector maps were generated by the Spatiotemporal Image Correlation Spectroscopy[70] (STICS) plugin previously implemented for detecting cytoplasmic flows in mouse oocytes[71] and available on https://research.stowers.org/imagejplugins/. The maps show cytoplasmic flow velocity magnitude and direction. Bright-field time-lapse images (Δt=0.5 s) were converted to 32-bit format, realigned using the Fiji StackReg plugin, and masked specifically around the oocyte contour before launching the STICS map jru V2

plugin with box-checking of output velocities, movie mask use, and a time correlation shift of 3 frames.

Immunocytochemistry. All immunocytochemistry images spanned 40–50 μm (Δz = 0.5 μm) to include the entire ~30 μm wide nucleus and were examined in 3D. Condensate numbers and surfaces were quantified on z-projections covering the entire nucleus for mouse/*Drosophila* nuclear speckles, on z-projections covering the entire condensate signal for Coilin and TDP-43, and on single z-planes for the nucleolus. The maximal radius of nuclear speckles or nucleoli served to calculate their volume. In Control and mutant SN oocytes from the FMN2 mouse strain, 20 to 30% of cells do not present nuclear speckles or any EU incorporation. Total nucleoplasmic signal intensities of condensate markers, corresponding to the sum of condensed and dissolved phases, were quantified on z-projections covering the entire nucleus and normalized by cytoplasmic background signal intensity.

Total nucleoplasmic signal intensities of SF3b155 and pSF3b155 (pThr313) were quantified on z-projections covering the entire nucleus and normalized by cytoplasmic background signal intensity. The total signal intensity of pSF3b155 (pThr313) in nuclear speckle droplets was measured on z-projections covering single droplets, thus integrating the intensity within the droplet volume, and normalized by an equally sized nucleoplasmic signal of pSF3b155 (pThr313) in a region devoid of nuclear speckles and DNA. Nucleoplasmic pSF3b155 (pThr313) was predominantly composed of either droplet-associated or chromatin-associated signals; signal ratios of droplet-associated to chromatin-associated pSF3b155 (pThr313) were obtained from single z-sections. We documented that: cytoplasmic force intensification in oocytes drove an increase in nuclear speckle droplet mobility all over the nucleoplasm in absence of apparent chromatin association; an important transcriptional drop accompanied chromatin compaction in these final stages of oocyte growth; and that the large majority of active splicing signal by the end of growth occurred in nuclear speckle droplets, which are compartments proposed to be sites of spliceosome accumulation for post-transcriptional splicing completion[33,34]. We, therefore, speculate that, by the end of oocyte growth, splicing activity is predominantly post-transcriptional.

Cytoplasmic actin filament (stained with Phalloidin) density was quantified with the Fiji Tubeness plugin. The plugin calculates a score of how much local pixels represent a tube based on the eigenvalues of the Hessian matrix, with high-intensity pixels corresponding to tubular structures and thus, correspond to actin filaments. The plugin also applies a watershed algorithm to measure the average size of the signal void in between the filaments. We verified the expected inverse relation between actin filament density and signal void in our data. Twenty measurements of cytoplasmic regions of 10 μm × 20 μm were made per oocyte on different apico-basal z-planes to maximally cover the entire cytoplasm.

Oocyte volumes were calculated with measured radii values. Nuclear volumes were defined by the external boundaries of the dissolved-phase SRSF2/SC35 signal that occupies the entire nucleoplasm. Briefly, the nucleus was segmented from z-stacks with a Fiji plugin based on signal intensity thresholding of individual z-planes and reconstructed as a 3D-ellipsoid by calculating the minimal-volume enclosing ellipsoid of the thresholded pixels; center position and volume were then calculated from the fitted ellipsoid. The surface occupied by chromatin was quantified on z-projections covering the entire DAPI signal.

In summary, numerous parameters tested in fixed Control and FMN2-mutant oocytes were comparable. This includes cell growth (i.e., cell size, which is also a readout of transcript accumulation in oocytes), nucleus volume, nuclear lamin A/C and g-actin levels[11], total nuclear protein levels of diverse nuclear condensate markers, the total volume of condensates per nucleus, and EU incorporation as a readout of nascent RNA transcription. This indicates that these parameters are

not implicated in splicing changes observed in late-growth FMN2$^{-/-}$ oocytes.

Droplet tracking. Time-lapse images of oocytes expressing SRSF2-GFP were corrected for bleaching with the histogram matching method and realigned with the Fiji StackReg plugin before proceeding with the SRSF2-GFP droplet center tracking using the Fiji Manual Tracking plugin. Temporal Mean Square Displacements (MSD) were calculated from 20 s droplet trajectories. Curves were fitted with the Nelder-Mead method using R software to estimate the diffusion exponent alpha (α). As the diffusion was found to be anomalous ($\alpha < 1$), we measured the "effective" diffusion coefficient to be able to compare the different conditions. The effective diffusion coefficient D_{eff} was calculated from a linear fit on the 40 first points (20 s) of the temporal MSD curve and normalized by droplet size (D_{eff} in $\mu m^2 s^{-1} \times \frac{3}{2}\pi r$ in μm). Although chromatin in fully-grown SN FMN2$^{-/-}$ oocytes is slightly less condensed than in Controls[11] and may thus interfere with droplet diffusion, Taxol or Nocodazole treatments did not affect the observable chromatin condensation state when compared to Controls, thus eliminating the potential chromatin-based bias. In long timescale 3D-tracking, droplet trajectories were corrected for drift with the nucleus centroid trajectories, and displacement distances were squared in graphs. For SRSF2-GFP droplet number and size evolution in NSN oocytes, droplets were manually counted in 3D on every timepoint, and maximal droplet surfaces were measured on first and last timepoints. Chromatin (H2B-RFP) surface evolution was quantified in the same NSN cells on 40 μm z-projections covering the whole signal and on every timepoint.

Droplet surface fluctuations. Droplet contour evolution in time was measured with a custom-built plugin Radioak for use in Fiji and available on https://github.com/gletort/ImageJFiles/tree/master/radioak. The plugin extracted the values of radii of a given selection for all angles around the selection center. Shape variation over time was measured by comparing the value of the radius relative to its average value for each angle. In Fig. 4a (upper right), contour fluctuation dynamics were represented visually with a color code: orange if the radius increased or decreased relative to the previous timepoint and white if stable when compared to a given threshold.

In all conditions, SRSF2-GFP droplets of comparable sizes (radius range from 2 to 2.7 μm) were selected. Time-lapse images spanning 15 s ($\Delta t = 0.5$ s) were cropped, realigned with the Fiji StackReg plugin, smoothened, and signal thresholded (dark background; default method). The generated binary droplet mask was then analyzed using the Analyze Particles option and the output was saved in zip format for Radiak. Radiak was subsequently launched with 1° angle increments from 0 to 360° (input of 360) and the radii values were extracted. For each angle, the mean radius "R" overall 30 timepoints was subtracted from the droplet radius "r" for each timepoint. The variance (r-R)^2 in μm^2 corresponds to the measure of droplet surface fluctuations that was plotted.

FRAP. FRAP image sequences were realigned with Fiji StackReg and SRSF2-GFP droplets within the region of interest were selected for fluorescence recovery analysis. Recovery was measured as fluorescence intensity of photobleached droplet corrected for background and normalized by the droplet's prebleach intensity. Recovery curves were rescaled from zero (bleach value) to one (100% recovery) and were fit to a simple exponential function (one-phase association) with Prism. Similar to (ref. 72), the recovery timescale (tau; τ) was extracted to calculate the apparent diffusion coefficients (D_{app}) of droplets with a radius r as $D_{app} \sim r^2/\tau$. Mobile fractions were determined as fluorescence intensity recovery fractions at 120 s for NSN and at 60 s for SN oocytes, which correspond to Control curve plateaus.

Biophysical model

Here, we briefly present a theoretical framework that provides a physical basis for interpreting the observations reported in this study. In (ref. 9), we described the oocyte cytoplasm as a fluid actively driven out of equilibrium by actomyosin-based mechanical forces. This activity, whereby chemical energy was converted to random active forces, triggered the active diffusion of tracer particles (vesicles) in the cytoplasm. This could be quantified by the mean squared velocity $\langle v^2 \rangle$ obtained from PIV analyses and was found to be larger than classical thermal diffusion. We argued in (refs. 9, 11) that over diffusion timescales across the oocyte, the cytoplasmic activity could be interpreted as an effective temperature in the cytoplasm defined by $T_c \propto \langle v^2 \rangle$. In (ref. 11), we proposed that cytoplasmic activity enhanced fluctuations of the nuclear membrane, which acted as a mechanical transducer, transmitting cytoplasmic active forces to the nuclear interior in the form of effective stirring of the nucleoplasm. This stirring resulted in the active diffusion of chromatin and the chromatin-embedded nucleolus[11], and could again be interpreted as an effective temperature defined by $T_n \propto \langle v_n^2 \rangle$, where v_n is the velocity of intranuclear tracer particles.

Consistent with these earlier findings, we report here that cytoplasmic activity triggered the active diffusion of micron-scale nuclear liquid-like condensates, thereby significantly accelerating their coalescence dynamics. The following scaling argument supports this mechanism. As a readout of the cytoplasmic active forces that are effectively transduced to the nucleoplasm, we use the instantaneous velocity of the nuclear membrane, which can be accessed experimentally: $v_{nm} \sim 0.3$ $\mu m/s$ in SN oocytes. We denote a the typical lateral extension of such active deformation of the nuclear membrane, which acts as a localized fluctuating source that stirs the nucleoplasm, and $l \sim 2.7$ μm its mean amplitude, measured experimentally in SN oocytes. Assuming, in a first approximation, a viscous nucleoplasm, a single fluctuating active source at the nuclear membrane acts as a Stokeslet of random direction and intensity and induces a long-range fluctuating flow in the nucleoplasm such that $\langle v_{st}^2(r) \rangle \sim v_{nm}^2 a^2/r^2$, where r denotes the distance from the source, and $\langle . \rangle$ the average over the fluctuating dynamics of the active source. Note that here $\sim$ means proportionality with a dimensionless coefficient of order 1. We next consider that cytoplasmic activity effectively induces a uniform density $c \sim 1/a^2$ of independent active sources on the nuclear membrane, which is assumed to be spherical. Here independence of the sources assumes that correlations induced by tension and bending of the nuclear membrane are negligible, which holds for sufficient activity. Summing the contribution of all sources, the fluctuations of the nucleoplasmic flow at a given point at a distance $r_0 = uR$ from the center of the nucleus (of radius R) can be obtained after standard algebra as in Eq. (2):

$$\langle v^2(u) \rangle \sim \frac{v_{nm}^2}{u} \ln \frac{1+u}{1-u} \qquad (2)$$

Averaging the next overall points in the nucleus shows finally that cytoplasmic activity, transduced by the nuclear membrane, causes a fluctuating flow within the nucleus such that $\langle v_{nu}^2 \rangle \sim v_{nm}^2$, where numerical prefactors of order 1 are omitted.

Importantly, the resulting flow spans the entire nucleus (independently of its radius), and has the same order of magnitude as the active sources localized at the nuclear membrane. The impact of such fluctuating flow on the dynamics of nuclear condensates can be quantified by the Peclet number $P_n = v_{nu} l/D_n$, where D_n is the mean value of the diffusion coefficient of nuclear condensates. The above orders of magnitude, together with the measured $D_n \sim 0.16$ $\mu m^2/s$ in SN oocytes, yields $P_n \sim 5$, which is consistent with an effective diffusion of active origin. Of note, the same analysis applies to molecular transport in the nucleoplasm, taking instead of D_n the diffusion coefficient D_m of molecular markers (dissolved SRSF2-GFP), which we measured by

FRAP in SN oocytes. Similarly, we found D_m -0.3 $\mu m^2/s$ and thus P_n-2.5, consistent with an effective diffusion of active origin at the molecular scale in the nucleoplasm. Finally, this shows that cytoplasmic activity can be transduced within the nucleoplasm via a simple, passive (i.e., without further energy supply) physical mechanism, which enhances the diffusion of nuclear condensates and nucleoplasmic molecules.

Furthermore, we report that the cytoplasmic activity was also transduced down to molecular scales within condensates. Indeed, the liquid-like condensates displayed increased surface fluctuations (consistent with a large effective intranuclear temperature T_n), as well as a faster turn-over of their molecular content, which supposedly facilitated the biochemical processes hosted by the condensates, which in our case correspond to mRNA splicing. The instantaneous velocity of the droplet interface could be estimated from experimental data as v_d- 0.9 micron/s in SN oocytes. The fact that v_d is of comparable order of magnitude to v_{nu} suggests that droplet surface fluctuations are imposed by shear forces in the nucleoplasm, while capillary forces are negligible. In turn, such surface fluctuations drive flows within droplet condensates; the impact of such flows on molecular dynamics can be, as above, quantified by a Peclet number $P_d = v_d\, l_d\, /D_d$, where l_d is the amplitude of fluctuations of the droplet interface and D_d the diffusion coefficient inferred from FRAP experiments in SN oocytes. Experimental values yield l_d -0.5 μm and D_d-0.3 $\mu m^2/s$ so that P_d-1.5, which is consistent with an effective diffusion of active origin at the molecular scale within nuclear liquid-like condensates.

Altogether, our observations suggest an energy cascade triggered by the cytoplasmic actomyosin activity, transduced by the nuclear membrane to the nucleoplasm causing active diffusion and coalescence of liquid-like condensates, and eventually transduced to the liquid-like condensate surface and interior, observed through condensate surface fluctuations and internal molecular turn-over. Based on this physical picture, it can be hypothesized that, due to energy dissipation, the contribution of active forces to fluctuations diminishes along this cascade from the cytoplasm to intranuclear liquid condensate interiors[73]. While we argued above that such energy cascades could, in principle, occur without extra energy inputs, additional, active mechanisms cannot be ruled out.

Computational models and 3D-simulations

Agents. To simulate the diffusion of nuclear droplets, we adapted 3D agent-based simulations from our previous work[12] implemented in C++; also see (refs. [74], [75]) for analytical modeling. We chose an agent-based framework for its flexibility, allowing us to test and compare directly different scenarios (chromatin presence, chromatin compaction, nucleus shape…). We defined three different types of agents: nuclear speckle-like (SRSF2$^+$) droplets, a single nucleolus of fixed size, and chromatin-like obstacles. To simplify the model, each agent was represented as a sphere determined by its center position and radius. Mobility analyses of the droplets and the nucleolus in the experiments revealed sub-diffusive motion inside the nucleus and, thus, obstacles were used to simulate molecular crowding in the nucleus. Nuclear obstacle amounts were based on experimental chromatin surface measurements. Potential droplet neo-nucleation and dissolution were excluded from simulations for simplicity. As observed experimentally, droplets could undergo collision-coalescence.

Confinement in the nucleus. All agents were confined inside a static spherical boundary representing the nuclear membrane. The confinement inside the nucleus was modeled as a repulsive force effective as soon as the agent was in contact with the membrane (see refs. [12], [76]).

Agent diffusion. Each agent was presumed to diffuse randomly (Brownian motion) and their velocity was dampened by nucleoplasmic friction. Droplet mobility was assumed to obey Stokes' law after verifying experimentally that the relation between SRSF2-GFP droplet

velocity and their size was coherent with this law. In continuity with our previous work[11], we modeled the effect of the cytoplasmic stirring activity on the agent diffusion coefficient inside the nucleus as in Eq. (3):

$$D = k_B(T + \alpha T_a)/\lambda = D_0 + \alpha D_a \qquad (3)$$

where D_a is the normalized activity-induced diffusion and D_O is the diffusion without activity. The values of D_O and α were estimated by linear regression on the effective diffusion coefficients of the nucleolus relative to cytoplasmic stirring activity shown in the supplementary data of ref. [11].

Agent contacts. Contact between agents depended on their type.

-Obstacle or nucleolus with any agent type (droplet, nucleolus, obstacle): contact between two spheres created a hard-core repulsive force to avoid physical overlap, as in refs. [12], [77]. Repulsion strength increased with sphere overlap, accounting for the limited compressibility of the biological objects[78].

-Droplet with droplet: droplets coming into close proximity coalesced as soon as they collided, consistent with experimental SRSF2-GFP data. Due to this biological rapidity of SRSF2-GFP droplet coalescence, we rendered coalescence instantaneous in simulations. The coalescing spheres were then replaced by a single sphere with a volume corresponding to the sum of the two original sphere volumes in order to conserve the initial mass.

Agent motion. The overall motion of each agent was determined by the balance of all forces it experienced: its intrinsic motility, its contact with other agents, and its contact with the nuclear membrane[12], as in Eq. (4):

$$\vec{v}_i = \frac{1}{n_i}\left(\sum_j \vec{F}_a(i,j) + \vec{F}_{ci} + \vec{B}_i\right) \qquad (4)$$

with $\eta_i = 6\pi r i \gamma$ as the friction coefficient opposing agent motion and calculated according to Stokes' law, and where γ is the viscosity of the medium, F_a is the interaction between agents (hard-core repulsion or attraction), F_c is the force of confinement inside the nucleus, and B_i is the Brownian motion with a diffusion coefficient determined by the cytoplasmic activity.

Cytoplasmic activity in Controls ± pharmacological inhibitors and mutants. The main effect of the conditions tested in experiments (Control + Nocodazole, Control + Taxol, FMN2$^{-/-}$) was assumed to be the shift in cytoplasmic forces transmitted into the nucleus. In simulations, only the value of the cytoplasmic activity was therefore tuned to mirror these experimental conditions. The values for SN oocytes were all based on experimental data[11] with Controls being 1, Controls +Nocodazole being 1.9, and FMN2$^{-/-}$ oocytes being 0.2. The values for NSN oocytes were based on the measurements of NSN Control nuclear membrane fluctuations, done as previously[11] and shown in Supplementary Fig. 1j, and with a value estimated at 0.55. The activities of the other biological conditions (inhibitors or mutant) for NSN oocytes were assumed to have a Control-like ratio of activity between SN and NSN oocytes corresponding to a factor of 1.8.

Long timescale simulations. In long timescale simulations, we added the possibility for obstacles to adhere compactly to the nucleolus similar to how chromatin condenses around the nucleolus in physiological conditions of oocyte growth. The obstacles were subsequently constrained to a fixed position relative to the nucleolus whose mobility they follow, and were only permitted small random fluctuations around this position. This allowed us to simulate three different nucleus configurations and test the effect of chromatin

compaction on nuclear droplet dynamics. The following simulation series with different nuclear states and a wide range of starting point cytoplasmic stirring activities were performed:

-NSN-like state (simulation series 1): obstacles were widely spread in the nucleoplasm and the starting point intensity of cytoplasmic activity was maintained constant throughout the simulation.

-NSN-like to SN-like transition state (simulation series 2): simulations were first in the NSN-like state with all obstacles widely spread and with low agent mobility. Then at 12 h, 40% of obstacles closest to the nucleolus were attracted towards and adhered to the nucleolus, mimicking chromatin condensation that occurs as of the Trans-stage into the SN stage. The percentage of obstacles that adhere to the nucleolus was roughly estimated from experimental measurements of the occupied surface of SN chromatin relative to NSN chromatin. Also, cytoplasmic activity at 12 h was multiplied by 1.8 times to consider the spike of activity measured in experimental conditions during the NSN to SN transition. The transition estimate of 12 h was defined by the largest number of SRSF2 droplets quantified in the nucleus of a Control Trans-staged oocyte (Supplementary Fig. 4a). Due to assimilation of both chromatin condensation and cytoplasmic force intensification, we consider this simulation series with a starting point activity of 0.55 to be the most representative of nuclear droplet kinetics during the physiological end of oocyte growth (Control NSN to SN).

-SN-like state (simulation series 3): 40% of the obstacles adhere to the nucleolus while the remaining 60% remain spread out. Starting point intensity of cytoplasmic activity is maintained constant throughout the simulation.

Droplet dynamics were simulated for 20 h (simulation series 1 and 3) or for 40 h (simulation series 2) with longer-term dynamics (up to 100 h) predicted by a decreasing exponential fit calculated from the last 5 h of the simulations.

FMN2-mutant oocyte specificities of nuclear shape and chromatin compaction. In simulations of the main manuscript, we explicitly model FMN2$^{-/-}$-like cytoplasmic stirring intensity with Control-like nucleus shapes and chromatin compaction to predict the time necessary to reach a four-droplet state, which corresponds to 59 ± 8 h. However, fully-grown SN FMN2$^{-/-}$ oocytes also present a less spherical nucleus shape due to microtubules nucleated from the microtubule organizing centers[11]. These SN oocytes also present a ~10% less compact chromatin than Controls[11] in a nucleus of comparable volume. Chromatin compaction in mutant NSN and Trans oocytes is comparable to Controls. We, therefore, assessed the effect of these two supplementary differences (nuclear shape and chromatin decompaction) on droplet dynamics in additional 3D simulations. We found that nuclear shape does not affect droplet dynamics in the context of Control-like cytoplasmic activity, as the time necessary to reach the four-droplet state remained comparable (Control-like cytoplasmic activity, nucleus shape, and chromatin compaction $t = 15 \pm 8$ h; Control-like cytoplasmic activity and chromatin compaction with FMN2$^{-/-}$-like nucleus shape $t = 18 \pm 6$ h). In contexts of FMN2$^{-/-}$-like cytoplasmic activity, a 10% less condensed chromatin slightly increased the time necessary to reach 4 droplets, and a less spherical nuclear shape increased the time further (FMN2$^{-/-}$-like cytoplasmic activity with Control-like nucleus shape and chromatin compaction $t = 59 \pm 8$ h; FMN2$^{-/-}$-like cytoplasmic activity and chromatin compaction with Control-like nucleus shape $t = 87 \pm 0.5$ h; FMN2$^{-/-}$-like cytoplasmic activity and nucleus shape with Control-like chromatin compaction $t > 100$ h). Merging all three FMN2$^{-/-}$-like properties together also significantly increased the time necessary to reach the four-droplet state (FMN2$^{-/-}$-like cytoplasmic activity, nucleus shape, and chromatin compaction $t > 100$ h). With the additional layers of complexity, these results provide more precise predictions of droplet dynamics in the most "realistic" version of an

FMN2-mutant oocyte. Nevertheless, we excluded these data from the computational section of the main manuscript for simplicity and primary focus on the consequences of cytoplasmic forces on nuclear droplet dynamics with Control-like parameters of nucleus shape and chromatin compaction during oocyte growth.

Parameter values and sources.

Agent/ Parameter	Value	Source/Information
Nucleus		
Radius	12 μm	Experimental measurements
Nucleolus		
Radius	4.5 μm ±0.2	Experimental measurements
Friction	1	Empirical to obtain diffusion coefficients similar to experimental measurements of nucleoli in Control NSN oocytes
Nucleus repulsion	30	Strength of confinement; empirical to avoid objects leaving the nucleus while allowing small deformation
Sphere repulsion	30	Strength of hard-core repulsion with other agents
Droplet		
Initial radius	0.9 μm ± 0.01	Experimental measurements of nuclear speckles in NSN oocytes
Initial number	55	Experimental quantifications of nuclear speckles in NSN oocytes
Nucleus repulsion	30	Strength of confinement; empirical to avoid objects leaving the nucleus while allowing small deformation
Sphere repulsion	10	Hard-core repulsion with other agents; empirical, with values moderated to allow small deformation
Fusion speed	Instantaneous	Simplification based on experimental observations
Friction	0.55	Empirical to obtain diffusion coefficients similar to experimental measurements of speckles in Control NSN oocytes
Obstacle		
Radius	0.85 μm ± 0.4	Empirical to confine nucleolus and speckle motion and to obtain similar diffusion coefficients and anomalous MSD exponents as in NSN experiments
Initial number	875	Empirical to confine nucleolus and speckle motion and to obtain similar diffusion coefficients and anomalous MSD exponents as in NSN experiments
Nucleus repulsion	30	Strength of confinement; empirical to avoid objects leaving the nucleus while allowing small deformation
Sphere repulsion	30	Hard-core repulsion with other agents; an empirical value equal to the nucleolus value
Friction	5	Empirical to have lower mobility when compared to other agents
Proportion contact	0 initial 0.4 after switch	Evaluated from experimental NSN vs. SN chromatin area in experiments
Simulation		
Time step	0.01 s	For numerical stability
Transition time	12 h	Time when simulation state switches from NSN-like to SN-like
Minimal mobility D_0	0.01	Calculated by linear regression of nucleolus diffusion relative to cytoplasmic stirring[11]
Coefficient of mobility α	0.11	Calculated by linear regression of nucleolus diffusion relative to cytoplasmic stirring[11]

RNA-sequencing, bioinformatics, and RT-qPCR

RNA extraction and sequencing. Mouse oocyte RNA extraction and sequencing were performed previously[11] and can be accessed on the Gene Expression Omnibus (accession number, GEO:GSE103718).

Exon usage analysis. For each sample, between 4 and 15 million reads were mapped to the mm10 reference genome using the splice-aware alignment program Hisat2 (ref. [79]) (IUC Galaxy wrapper hisat2 v2.1.0). The differential exon usage expression analysis was based on DEXSeq[80]. Briefly, we used the DEXSeq *prepare_annotation.py* script from the Conda environment bioconductor-dexseq==1.28.1 to generate pseudo exons (exon-bins) by in silico segmentation of genes using the Ensembl mm10 gene annotation file Mus_musculus.GRCm38.83.chr.gtf. The relative abundance of each exon-bin was calculated with the DEXSeq-Count algorithm by counting all sequenced reads assigned to each exon-bin. Exon-bins related to multiple genes were excluded from further analysis. Finally, the differential usage of exon-bins between FMN2$^{+/-}$ and FMN2$^{-/-}$ conditions was done with DEXSeq (IUC Galaxy wrappers DEXSeq and DEXSeq-Count, v1.24.0.0). Differentially used exon-bins with a Benjamini–Hochberg adjusted *p* value (P_{adj}) threshold of 0.05 were extracted into sheet 1 of Supplementary Data 1 and selected for further RT-qPCR and exon-bin size analyses. Exon-bin sizes in sheet 2 of Supplementary Data 1 were plotted relative to their over- or under-representation in FMN2$^{-/-}$ oocytes ($P_{adj} < 0.05$). Exons from protein-coding transcripts for RT-qPCR validation were selected according to high fold changes (>2) and low P_{adj} (<0.05).

Isoform usage analysis. Transcript isoform abundance quantifications were obtained with RSEM[81], which uses Bowtie2 (ref. [82]) for alignment with a custom index built from the mm10 reference genome and the GTF file Mus_musculus.GRCm38.83.chr, and then computes the expression abundance for each isoform (RSEM, ARTbio Galaxy wrapper, Version 0.9.0). Isoform differential expression analysis between FMN2$^{+/-}$ and FMN2$^{-/-}$ conditions was performed for expressed genes (TPM >1) with more than one isoform using the R package IsoformSwitchAnalysisR[83] (iSAR), which uses counts generated by RSEM and the DEXSeq algorithm to calculate the differential usage of isoforms. Supplementary Data 2 contains the lists of differentially used isoforms with an FDR-adjusted *P*-value (False Discovery Rate) threshold of 0.05, alternative splicing events per transcript, splicing coordinates, and isoform switch consequences. Differential isoforms generated by exon skipping from a single gene similarly expressed in Controls and Mutants were chosen for RT-qPCR validation of alternative splicing. Using this approach, we detected 1259 transcripts with altered splicing patterns in FMN2$^{-/-}$ oocytes (Supplementary Data 2), which probably start appearing by the end of growth as of the Transstage when splicing changes assessed by pSF3b155 become visible (Fig. 4d, e). This number of transcripts is coherent with studies reporting ~7000 to 11,000 expressed genes during the whole process of mouse oocyte growth[84,85].

Enrichment and spatial correlations of SRSF1 and SRSF2 binding sites. SRSF1 and SRSF2 binding sites were obtained from ref. [38] for binding site enrichment analyses. The numbers of SRSF1 and SRSF2 binding sites in differentially used exons (DEXSeq) or transcripts (iSAR) were then compared to the number of SRSF1 and SRSF2 binding sites in all genes. Correlation tests of distance metrics between genomic features were implemented using the GenometriCorr package[86], which computes spatial association of datasets to highlight potentially relevant relationships between them. We compared sites of differential exon usage (DEXSeq) or alternative splice sites (iSAR) with binding sites of SRSF1, SRSF2, MBNL3, and YY1[38–40]. Two in silico controls were also generated (Prom50 and Term50), which correspond to the first and last 50 nucleotides of all RefSeqNCBI transcripts, respectively.

All Jaccard measures were significant ($P < 0.02$) except for the overlap between differentially used exon sites and Prom50 sites. When necessary, datasets were converted to the Ensembl mm10 gene annotation using the IUC Galaxy wrapper crossmap.bed v0.5.2 + galaxy0 (http://crossmap.sourceforge.net).

Gene ontology and analyses of the translational status of transcripts. The list of genes affected by differential exon (DEXSeq list) or isoform usage (iSAR list) were merged for functional enrichment analyses and for comparative analyses with transcripts translated during the first meiotic division (Supplementary Data 4, 5). Biological processes and Gene Ontologies were analyzed using Enrichr[87,88] available through the web interface https://maayanlab.cloud/Enrichr/. The full lists of translated, activated (engaged in translation), and repressed (degraded) transcripts were kindly shared by Marco Conti and based on their previous work[46]. Their probe set GeneID's were updated and converted using the Mouse Genome Informatics website (http://www.informatics.jax.org/batch) before comparison with the FMN2$^{-/-}$ list of genes shown in Supplementary Data 5.

RT-qPCR. Total cellular RNA (25 oocytes per sample) was extracted with the RNAqueous-Micro Total RNA Isolation Kit (AM1931; Thermo Fisher) following the manufacturer's protocol and eluted into 20 µl of elution buffer before DNAase I treatment. cDNA was synthesized using the iScript Reverse Transcription Supermix (1708840; Bio-Rad) and the quantitative PCR was performed in triplicate with primer pairs (listed below) in a CFX96 Touch Real-Time PCR Detection System (Bio-Rad) followed by an analysis of the CFX Maestro Software (Bio-Rad). Samples were normalized to that of Rpl19 (Ribosomal protein L19) and Gapdh (Glyceraldehyde 3-phosphate dehydrogenase), and relative fold changes were calculated using the $2^{-\Delta\Delta c}$ method. For DEXSeq exon usage validation with RT-qPCR, we designed the two primers against the same exon detected as differentially used by DEXSeq. The expression of the total transcript was verified (except for Kctd20) with primer pairs against junctions of constitutive exons, which were not classified as differentially used by DEXSeq. The general primer design strategy is illustrated in sheet 2 of Supplementary Data 1. For iSAR isoform usage validation with RT-qPCR, we designed isoform-specific primer pairs against exon 2–3 and exon 4 for the long isoform and exon 2 and exon 3–6 for the short isoform, as illustrated in sheet 5 of Supplementary Data 2.

The following primers were used:

Ercc5 (ENSMUSE00000812268) forward primer (5′to3′) F=TCT AAGGAGAGGAACTCAGGGG, reverse primer (5′to3′) R=TCTGCTA-GATCATCACTGCTGC; Ercc5 (NM_011729.2) F=GCGTCCTTTATCC-TAACGGGA, R=GCCAAATGCTAATATCCACGGC; Hnrnpdl (ENSMUSE00000825422) F=TCTATCTCTGGGGGTCGCAC, R= CTTTACGCTGGT ACATGAAGTTGG; Hnrnpdl (XM_036165266.1) F=ATAGGTTCTGGGA AGTGCGA, R=TTGGTTCCAGTTTTGGCCCT; Kctd20 (ENSMUSE0000 0788494) F=AGATCAAGAGGAGACCTGGCG, R=ACATGGCGACTCTTT CCTTCC; Ncapg2 (ENSMUSE00000266378) F= TCATCCATGTCA TCCGCCAC, R= TGGCATTCTCCTTCTCGCATT; Ncapg2 (NM_133762.4) F= GGACCTGATGCAGACTACGG, R=AGGGAGCCTTACAACCCCAG; Ogdh (ENSMUSE00001059524) F=TTAAGGCCATTGACAGCCTCC, R=TACAGGTGCAGAATAGCACCG; Ogdh (NM_001252283.1) F=CCCCT TTCCCTGAGTCGAAG, R=TGGTGACCCCTGACCTGATA; Exosc1 isoform 1 (NM_025644.4) F=AGAATGGCGCGGTTCCC, R=GGCAAACCG TGAGTTGATGC; Exosc1 isoform 2 (NM_001164561.1) F=TGAAGA CCAGCGAGAATGGC, R=AATTTCTACCTTACAGGTGACGAC.

Data availability

All data generated in this study are provided in the main manuscript, Supplementary Information, and Source Data files. All figures have associated raw data in the Source Data file. There are no restrictions on data availability. Parameter configuration files used to generate the

simulations with our open source code are available on https://github.com/gletort/Esfera in the 'parameters' folder. This study used publicly available data. Mouse oocyte RNA extraction and sequencing were performed in ref. 11, and can be accessed on the Gene Expression Omnibus (accession number, GEO:GSE103718). Bioinformatics in this manuscript were handled by the IBPS ARTbio bioinformatics platform (www.ibps.sorbonne-universite.fr/fr/actus/actus/6919,artbio-bioinformatique) and RNA-sequencing data analyses were performed with published approaches (see Methods). Other publicly available data include Enrichr (https://maayanlab.cloud/Enrichr/), Ensembl (www.ensembl.org/Mus _musculus/Info/Index), and Mouse Genome Informatics (www.informatics.jax.org).

Code availability

Code generated for this study is available on https://github.com/gletort/ImageJFiles/tree/master/radioak. Our source code C++ used for the simulations is open source and publicly available on https://github.com/gletort/Esfera (ref. 89). Other publicly available codes used are available on: https://github.com/Carreau/OOCytes/tree/0.9 (ref. 9) and https://research.stowers.org/imagejplugins (refs. 70,70). Code descriptions are in Methods.

References

1. Clift, D. & Schuh, M. Restarting life: fertilization and the transition from meiosis to mitosis. *Nat. Rev. Mol. Cell Biol.* **14**, 549 (2013).
2. Brunet, S. & Maro, B. Germinal vesicle position and meiotic maturation in mouse oocyte. *Reproduction* **133**, 1069–1072 (2007).
3. Levi, M., Ghetler, Y., Shulman, A. & Shalgi, R. Morphological and molecular markers are correlated with maturation- competence of human oocytes. *Hum. Reprod.* **28**, 2482–2489 (2013).
4. Binyam, M., Scheffler, K. & Schuh, M. Assembly and positioning of the oocyte meiotic spindle. *Annu. Rev. Cell Dev. Biol.* **34**, 381–403 (2018).
5. Pegoraro, A. F., Janmey, P. & Weitz, D. A. Mechanical properties of the cytoskeleton and cells. *Cold Spring Harb. Perspect. Biol.* **9**, a022038 (2017).
6. Guo, M. et al. Probing the stochastic, motor-driven properties of the cytoplasm using force spectrum microscopy. *Cell* **158**, 822–832 (2014).
7. Fakhri, N. et al. High-resolution mapping of intracellular fluctuations using carbon nanotubes. *Science* **344**, 1031–1035 (2014).
8. Chu, F. Y., Haley, S. C. & Zidovska, A. On the origin of shape fluctuations of the cell nucleus. *Proc. Natl Acad. Sci. USA* **114**, 10338–10343 (2017).
9. Almonacid, M. et al. Active diffusion positions the nucleus in mouse oocytes. *Nat. Cell Biol.* **17**, 470–479 (2015).
10. Ahmed, W. W. et al. Active mechanics reveal molecular-scale force kinetics in living oocytes. *Biophys. J.* **114**, 1667–1679 (2018).
11. Almonacid, M. et al. Active fluctuations of the nuclear envelope shape the transcriptional dynamics in oocytes. *Dev. Cell* **51**, 145–157 (2019).
12. Colin, A. et al. Active diffusion in oocytes nonspecifically centers large objects during prophase I and meiosis I. *J. Cell Biol.* **219**, e201908195 (2020).
13. Shin, Y. & Brangwynne, C. P. Liquid phase condensation in cell physiology and disease. *Science* **357**, 1–11 (2017).
14. Banani, S. F., Lee, H. O., Hyman, A. A. & Rosen, M. K. Biomolecular condensates: organizers of cellular biochemistry. *Nat. Rev. Mol. Cell Biol.* **18**, 285–298 (2017).
15. Lyon, A. S., Peeples, W. B. & Rosen, M. K. A framework for understanding the functions of biomolecular condensates across scales. *Nat. Rev. Mol. Cell Biol.* **22**, 215–235 (2021).
16. Miyara, F. et al. Chromatin configuration and transcriptional control in human and mouse oocytes. *Mol. Reprod. Dev.* **64**, 458–470 (2003).
17. Alberti, S. & Dormann, D. Liquid – liquid phase separation in disease. *Annu. Rev. Genet.* **53**, 171–196 (2019).
18. Li, W. et al. Biophysical properties of AKAP95 protein condensates regulate splicing and tumorigenesis. *Nat. Cell Biol.* **22**, 960–972 (2020).
19. Alberti, S. & Hyman, A. A. Biomolecular condensates at the nexus of cellular stress, protein aggregation disease and ageing. *Nat. Rev. Mol. Cell Biol.* **22**, 196–213 (2021).
20. Boija, A., Klein, I. A. & Young, R. A. Biomolecular condensates and cancer. *Cancer Cell* **39**, 174–192 (2021).
21. Lafarga, M. et al. Cajal bodies in neurons. *RNA Biol.* **14**, 712–725 (2017).
22. Francis, A. C. et al. HIV-1 replication complexes accumulate in nuclear speckles and integrate into speckle-associated genomic domains. *Nat. Commun.* **11**, 3505 (2020).
23. Hensel, N. & Claus, P. The actin cytoskeleton in SMA and ALS: how does it contribute to motoneuron degeneration? *Neurosci* **24**, 51–72 (2018).
24. Clark, J. A., Yeaman, E. J., Blizzard, C. A., Chuckowree, J. A. & Dickson, T. C. A case for microtubule vulnerability in amyotrophic lateral sclerosis: altered dynamics during disease. *Front. Cell. Neurosci.* **10**, 1–16 (2016).
25. Walsh, D. & Naghavi, M. H. Exploitation of cytoskeletal networks during early viral infection. *Trends Microbiol.* **27**, 39–50 (2019).
26. Naghavi, M. H. HIV-1 capsid exploitation of the host microtubule cytoskeleton during early infection. *Retrovirology* **18**, 1–11 (2021).
27. Bonnet-Garnier, A. et al. Genome organization and epigenetic marks in mouse germinal vesicle oocytes. *Int. J. Dev. Biol.* **56**, 877–887 (2012).
28. Sawyer, I. A., Sturgill, D. & Dundr, M. Membraneless nuclear organelles and the search for phases within phases. *Wiley Interdiscip. Rev. RNA* **10**, 1–20 (2019).
29. Kroschwald, S., Maharana, S. & Simon, A. Hexanediol: a chemical probe to investigate the material properties of membrane-less compartments. *Matters* 201702000010 (2017).
30. Lee, D. S. W., Wingreen, N. S. & Brangwynne, C. P. Chromatin mechanics dictates subdiffusion and coarsening dynamics of embedded condensates. *Nat. Phys.* https://doi.org/10.1038/s41567-020-01125-8 (2021).
31. Strickfaden, H. et al. Condensed chromatin behaves like a solid on the mesoscale in vitro and in living cells. *Cell* **183**, 1772–1784.e13 (2020).
32. Tripathi, A. K., Das, T., Paneru, G., Pak, H. K. & Tlusty, T. Acceleration of enzymatic catalysis by active hydrodynamic fluctuations. *Commun. Phys.* **5**, 1–11 (2022).
33. Girard, C. et al. Post-transcriptional spliceosomes are retained in nuclear speckles until splicing completion. *Nat. Commun.* **3**, 994 (2012).
34. Gordon, J. M., Phizicky, D. V. & Neugebauer, K. M. Nuclear mechanisms of gene expression control: pre-mRNA splicing as a life or death decision. *Curr. Opin. Genet. Dev.* **67**, 67–76 (2021).
35. Barutcu, A. R. et al. Systematic mapping of nuclear domain-associated transcripts reveals speckles and lamina as hubs of functionally distinct retained introns. *Mol. Cell* **82**, 1035–1052.e9 (2022).
36. Nilsen, T. W. & Graveley, B. R. Expansion of the eukaryotic proteome by alternative splicing. *Nature* **463**, 457–463 (2010).
37. Cossa, G. et al. Localized inhibition of protein phosphatase 1 by NUAK1 promotes spliceosome activity and reveals a MYC-sensitive feedback control of transcription. *Mol. Cell* **77**, 1322–1339.e11 (2020).
38. Pandit, S. et al. Genome-wide analysis reveals SR protein cooperation and competition in regulated splicing. *Mol. Cell* **50**, 223–235 (2013).

39. Poulos, M. G. et al. Progressive impairment of muscle regeneration in muscleblind-like 3 isoform knockout mice. *Hum. Mol. Genet.* **22**, 3547–3558 (2013).

40. Sigova, A. A. et al. Transcription factor trapping by RNA in gene regulatory elements. *Science* **350**, 978–982 (2015).

41. Kurogi, Y. et al. Identification of a chemical inhibitor for nuclear speckle formation: Implications for the function of nuclear speckles in regulation of alternative pre-mRNA splicing. *Biochem. Biophys. Res. Commun.* **446**, 119–124 (2014).

42. Kotake, Y. et al. Splicing factor SF3b as a target of the antitumor natural product pladienolide. *Nat. Chem. Biol.* **3**, 570–575 (2007).

43. Sharma, A., Takata, H., Shibahara, K., Bubulya, A. & Bubulya, P. A. Son is essential for nuclear speckle organization and cell cycle progression. *Mol. Biol. Cell* **21**, 650–663 (2010).

44. Ahn, E. Y. et al. SON controls cell-cycle progression by coordinated regulation of RNA splicing. *Mol. Cell* **42**, 185–198 (2011).

45. Ilik, I. A. et al. SON and SRRM2 are essential for nuclear speckle formation. *Elife* **9**, e60579 (2020). 1–24.

46. Chen, J. et al. Genome-wide analysis of translation reveals a critical role for deleted in azoospermia-like (Dazl) at the oocyte-to-zygote transition. *Genes Dev.* **25**, 755–766 (2011).

47. Dumont, J. et al. Formin-2 is required for spindle migration and for the late steps of cytokinesis in mouse oocytes. *Dev. Biol.* **301**, 254–265 (2007).

48. Azoury, J., Lee, K. W., Georget, V., Hikal, P. & Verlhac, M. Symmetry breaking in mouse oocytes requires transient F-actin meshwork destabilization. *Development* **2908**, 2903–2908 (2011).

49. Quinlan, M. E. Cytoplasmic streaming in the *Drosophila* oocyte. *Annu. Rev. Cell Dev. Biol.* **32**, 173–195 (2016).

50. Drechsler, M., Giavazzi, F., Cerbino, R. & Palacios, I. M. Active diffusion and advection in *Drosophila* oocytes result from the interplay of actin and microtubules. *Nat. Commun.* **8**, 1520 (2017).

51. Goldstein, R. E. & van de Meent, J. W. A physical perspective on cytoplasmic streaming. *Interface Focus* **5**, 20150030 (2015).

52. Gurdon, J. B. & Wilmut, I. Nuclear transfer to eggs and oocytes. *Cold Spring Harb. Perspect. Biol.* **3**, a002659 (2011).

53. Leader, B. et al. Formin-2, polyploidy, hypofertility and positioning of the meiotic spindle in mouse oocytes. *Nat. Cell Biol.* **4**, 921–928 (2002).

54. Verlhac, M. H., Kubiak, J. Z., Clarke, H. J. & Maro, B. Microtubule and chromatin behavior follow MAP kinase activity but not MPF activity during meiosis in mouse oocytes. *Development* **120**, 1017–1025 (1994).

55. Reis, A., Chang, H., Levasseur, M. & Jones, K. T. APC cdh1 activity in mouse oocytes prevents entry into the first meiotic division. *Nat. Cell Biol.* **8**, 539–540 (2006).

56. El-Hayek, S. & Clarke, H. J. in *Molecular Mechanisms of Cell Differentiation in Gonad Development* (ed. Piprek, R. P.) Ch. 8 (Springer, 2016).

57. Clarke, H. J. Regulation of germ cell development by intercellular signaling in the mammalian ovarian follicle. *Wiley Interdiscip. Rev. Dev. Biol.* **7**, 1–22 (2018).

58. Tsurumi, C., Hoffmann, S., Geley, S., Graeser, R. & Polanski, Z. The spindle assembly checkpoint is not essential for CSF arrest of mouse oocytes. *J. Cell Biol.* **167**, 1037–1050 (2004).

59. Terret, M. E. et al. DOC1R: a MAP kinase substrate that control microtubule organization of metaphase II mouse oocytes. *Development* **130**, 5169–5177 (2003).

60. Ribbeck, K. & Görlich, D. The permeability barrier of nuclear pore complexes appears to operate via hydrophobic exclusion. *EMBO J.* **21**, 2664–2671 (2002).

61. Strom, A. R. et al. Phase separation drives heterochromatin domain formation. *Nature* **547**, 241–245 (2017).

62. Flanagan, M. D. & Lin, S. Cytochalasins block actin filament elongation by binding to high affinity sites associated with F-actin. *J. Biol. Chem.* **255**, 835–838 (1980).

63. Schiff, P. B. & Horwitz, S. B. Taxol stabilizes microtubules. *Proc. Natl Acad. Sci. USA* **77**, 1561–1565 (1980).

64. Teng, T. et al. Splicing modulators act at the branch point adenosine binding pocket defined by the PHF5A–SF3b complex. *Nat. Commun.* **8**, 15522 (2017).

65. Jao, C. Y. & Salic, A. Exploring RNA transcription and turnover in vivo by using click chemistry. *Proc. Natl Acad. Sci. USA* **105**, 15779–15784 (2008).

66. Schuh, M. & Ellenberg, J. A new model for asymmetric spindle positioning in mouse oocytes. *Curr. Biol.* **18**, 1986–1992 (2008).

67. Bornschlögl, T. et al. Filopodial retraction force is generated by cortical actin dynamics and controlled by reversible tethering at the tip. *Proc. Natl Acad. Sci. USA* **110**, 18928–18933 (2013).

68. Paraschiv, A. et al. Influence of membrane-cortex linkers on the extrusion of membrane tubes. *Biophys. J.* **120**, 598–606 (2021).

69. Neuman, K. C. & Block, S. M. Optical trapping. *Rev. Sci. Instrum.* **75**, 2787–2809 (2004).

70. Hebert, B., Costantino, S. & Wiseman, P. W. Spatiotemporal image correlation spectroscopy (STICS) theory, verification, and application to protein velocity mapping in living CHO cells. *Biophys. J.* **88**, 3601–3614 (2005).

71. Yi, K. et al. Dynamic maintenance of asymmetric meiotic spindle position through Arp2/3-complex-driven cytoplasmic streaming in mouse oocytes. *Nat. Cell Biol.* **13**, 1252–1258 (2011).

72. Elbaum-Garfinkle, S. et al. The disordered P granule protein LAF-1 drives phase separation into droplets with tunable viscosity and dynamics. *Proc. Natl Acad. Sci. USA* **112**, 7189–7194 (2015).

73. Bernheim-Groswasser, A., Gov, N. S., Safran, S. A. & Tzlil, S. Living matter: mesoscopic active materials. *Adv. Mater.* **30**, 1–21 (2018).

74. Razin, N., Voituriez, R., Elgeti, J. & Gov, N. S. Generalized Archimedes' principle in active fluids. *Phys. Rev. E* **96**, 32606 (2017).

75. Razin, N., Voituriez, R., Elgeti, J. & Gov, N. S. Forces in inhomogeneous open active-particle systems. *Phys. Rev. E* **96**, 52409 (2017).

76. Letort, G. et al. PhysiBoSS: a multi-scale agent-based modelling framework integrating physical dimension and cell signalling. *Bioinformatics* **35**, 1188–1196 (2019).

77. Letort, G. et al. A computational model of the early stages of acentriolar meiotic spindle assembly. *Mol. Biol. Cell* **30**, 863–875 (2019).

78. Drasdo, D., Hoehme, S. & Block, M. On the role of physics in the growth and pattern formation of multi-cellular systems: What can we learn from individual-cell based models? *J. Stat. Phys.* **128**, 287–345 (2007).

79. Kim, D., Paggi, J. M., Park, C., Bennett, C. & Salzberg, S. L. Graph-based genome alignment and genotyping with HISAT2 and HISAT-genotype. *Nat. Biotechnol.* **37**, 907–915 (2019).

80. Anders, S., Reyes, A. & Huber, W. Detecting differential usage of exons from RNA-seq data. *Genome Res.* **22**, 2008–2017 (2012).

81. Li, B. & Dewey, C. N. RSEM: accurate transcript quantification from RNA-seq data with or without a reference genome. *BMC Bioinforma.* **12**, 1–16 (2014).

82. Langmead, B. & Salzberg, S. L. Fast gapped-read alignment with Bowtie 2. *Nat. Methods* **9**, 357–359 (2012).

83. Vitting-Seerup, K. & Sandelin, A. IsoformSwitchAnalyzeR: analysis of changes in genome-wide patterns of alternative splicing and its functional consequences. *Bioinformatics* **35**, 4469–4471 (2019).

84. Pan, H., O'Brien, M. J., Wigglesworth, K., Eppig, J. J. & Schultz, R. M. Transcript profiling during mouse oocyte development and the effect of gonadotropin priming and development in vitro. *Dev. Biol.* **286**, 493–506 (2005).

85. Sha, Q. et al. CNOT 6L couples the selective degradation of maternal transcripts to meiotic cell cycle progression in mouse oocyte. *EMBO J.* **37**, 1–19 (2018).

86. Favorov, A. et al. Exploring massive, genome scale datasets with the GenometriCorr package. *PLoS Comput. Biol.* **8**, e1002529 (2012).

87. Chen, E. Y. et al. Enrichr: interactive and collaborative HTML5 gene list enrichment analysis tool. *BMC Bioinforma.* **14**, 1–14 (2013).

88. Kuleshov, M. V. et al. Enrichr: a comprehensive gene set enrichment analysis web server 2016 update. *Nucleic Acids Res.* **44**, 90–97 (2016).

89. Letort, G. Cytoplasmic forces functionally reorganize nuclear condensates in oocytes. *Zenodo* https://doi.org/10.5281/zenodo.6854730 (2022).

Author contributions

A.A.J. and M.-H.V. conceived the project, which was supervised by M.-E.T. and M.-H.V. A.A.J. designed and performed all experiments on mouse oocytes with assistance from A.E and M.-H.V. for microinjections. G.L. performed 3D-computer simulations. F.-C.T. performed and analyzed optical trapping experiments. A.E. and C.D.S. performed RT-qPCR experiments. S.C. and J.-R.H. did all *Drosophila* oocytes experiments. A.A.J. analyzed all mouse and *Drosophila* experiments. A.A.J. directed the analyses of the RNA-seq data in collaboration with the IBPS ARTbio bioinformatics platform. C.A. performed and analyzed bioinformatical enrichment and spatial correlation analyses. N.S.G. and R.V. contributed to the physical modeling and participated in discussions on data interpretations. A.A.J. wrote the manuscript, which was seen and corrected by all authors.

Competing interests

The authors declare no competing interests.

Additional information

Supplementary information The online version contains supplementary material available at https://doi.org/10.1038/s41467-022-32675-5.

Correspondence and requests for materials should be addressed to Adel Al Jord.

Peer review information *Nature Communications* thanks the anonymous reviewer(s) for their contribution to the peer review of this work.

Reprints and permission information is available at http://www.nature.com/reprints

Publisher's note Springer Nature remains neutral with regard to jurisdictional claims in published maps and institutional affiliations.